Analytical initial conditions and an analysis of baroclinic instability waves in f- and β-plane 3D channel models

P. A. Ullrich,[a]* K. A. Reed[b] and C. Jablonowski[c]

[a]*Department of Land, Air and Water Resources, University of California, Davis, USA*
[b]*School of Marine and Atmospheric Sciences, Stony Brook University, NY, USA*
[c]*Department of Atmospheric, Oceanic & Space Sciences, University of Michigan, Ann Arbor, USA*

*Correspondence to: P. A. Ullrich, Department of Land, Air and Water Resources, University of California, Davis, One Shields Avenue, Davis, CA 95616, USA. E-mail: paullrich@ucdavis.edu

The article presents a description of idealized, balanced initial conditions for dry 3D channel models with either the hydrostatic or non-hydrostatic shallow-atmosphere equation set. Both the analytical expressions for an f- and β-plane configuration are provided and possible variations are discussed. The initialization with an overlaid perturbation is then used for baroclinic instability studies which can serve either as a test case for the numerical discretization or for physical science investigations such as the impact of the Coriolis parameter on the evolution of baroclinic waves.

Example results for two channel models are presented: the MCore and the Weather Research and Forecasting (WRF) models. The simulations show that the evolution of the baroclinic wave on the β-plane is more unstable than the corresponding f-plane configuration, experiencing a faster linear growth rate of the most unstable wave mode, a shorter most unstable wavelength, a narrower meridional width, and an earlier breaking of the baroclinic wave. A theoretical analysis based on linearized quasi-geostrophic (QG) theory sheds light on these findings. It is shown that the simulated baroclinic instability waves on both the f- and β-plane closely match the predicted wavelength, shape and linear growth rate obtained from the QG theory, thus validating the model results.

Key Words: baroclinic instability; dynamical core; test case; non-hydrostatic channel models; f- and β-plane; Coriolis parameter; linear quasi-geostrophic theory

Received 21 October 2014; Revised 8 May 2015; Accepted 14 May 2015; Published online in Wiley Online Library 14 July 2015

1. Introduction

Baroclinic waves are of fundamental importance in the Earth's atmosphere. They represent the synoptic-scale patterns of high and low pressure systems in the midlatitudes, and are the main exchange mechanism for energy and momentum between the tropical and polar regions. Baroclinic waves and baroclinic instabilty have therefore been of interest to the modelling community for decades, as documented by e.g. Schär and Wernli (1993) and previous authors listed therein. In particular, idealized simulations of different baroclinic wave life cycles, such as the cyclonic versus anticyclonic life cycle with the very different behaviour of the upper-air trough, have helped shed light on their dependence on the initial background conditions. Such life cycle aspects have, for example, been discussed by Simmons and Hoskins (1978) and Thorncroft *et al.* (1993), who used global spectral transform models in spherical geometry.

Besides global models, 3D channel models with either the f- or β-plane approximation of the Coriolis parameter are also popular tools to investigate the fundamental behaviour of baroclinically unstable flows. Channel models are often less expensive to run from a computational viewpoint, and provide

good representation of the midlatitudinal flow which is mostly governed by synoptic-scale sequences of high and low pressure systems. These are often closely approximated by quasi-geostropic theory. Therefore, a wide variety of equation sets have been used for channel models, ranging from the semi-geostrophic equations and primitive equations to the non-hydrostatic Euler equations with the shallow-atmosphere approximation. An issue that arises for all these equation sets is the choice of the initial conditions for baroclinic wave experiments. A typical initial state consists of a hydrostatically and geostrophically balanced atmosphere in thermal wind balance which is overlaid with a perturbation. This perturbation acts as a trigger for the evolution of the baroclinic wave.

Defining such a balanced initial base state is not necessarily straightforward since it needs to be a steady-state solution to the equation set. In addition, it needs to provide certain physical characteristics such as static stability and a zonal jet with strong vertical wind shear which makes the atmosphere baroclinically unstable. Furthermore, the initial state should be easy to generate, easy to modify and should allow exact reproducibility by other modellers. These criteria are at the very core of this article. They provide motivation for the definition of balanced initial

conditions for hydrostatic and non-hydrostatic channel models, which are built upon analytical expressions. These can be evaluated on any model grid and are versatile since they (e.g.) provide a switch between the f- and β-plane configurations for channel models. The initial conditions presented in this article can also be easily modified if other physical characteristics are desired, such as a meridional (barotropic) shear of the background zonal wind or the inclusion of moisture. This is important since the evolution of baroclinic instability waves depends on the background conditions as mentioned above, and a technique for the generation of flexible initial states opens up wide application areas.

Unfortunately, almost none of the initial states used in the published literature for baroclinic wave studies fulfill these criteria. A notable exception is the in-depth description of the balanced f-plane background state by Wang and Polvani (2011) which nevertheless still relies on numerical integrations and an iterative procedure for the overlaid perturbation. More recently, Terpstra and Spengler (2015) proposed a methodology which removes the need for iteration but still relies on numerical integration for constructing the basic state. The by-far dominant technique for channel models uses an f-plane configuration and prescribes a zonally invariant, constant, small potential vorticity (PV) value in the troposphere (like 0.4 PV units (PVU)) and a large PV value (like 4 PVU) in the stratosphere. In addition, a dividing line, such as a hyperbolic tangent profile in the meridional direction, is defined between the two regimes, before the 2D PV distribution is numerically inverted via an iterative technique and chosen boundary conditions. However, the resulting initial dataset is typically not fully balanced. Therefore, it is further smoothed in an iterative fashion. This technique is for example outlined in Zhang (2004), Plougonven and Snyder (2007) or Waite and Snyder (2009), and was inspired by the method in Rotunno (1994). Davis (2010) extended this PV inversion technique to allow for β-plane variations of the initial dataset in a moist environment. However, none of the groups disclosed the full details of their initializations so that their experiments cannot be easily reproduced. Furthermore, there is no agreement on the form of the overlaid perturbation. Some groups like Plougonven and Snyder (2007) or Waite and Snyder (2009) prefer an iteratively computed, unbalanced normal mode perturbation of the most unstable wave. Others like Zhang (2004) define a localized, balanced PV perturbation before the PV inversion is initiated.

The purpose of this article is twofold. First, we provide a thorough description of idealized, balanced, analytical and reproducible initial conditions for dry 3D channel models with hydrostatic or non-hydrostatic shallow-atmosphere equation sets. These can then be overlaid with a localized, unbalanced perturbation of (e.g.) the zonal wind field to initiate the growth of the baroclinic wave. Both an f- and β-plane configuration are described, which are anchored in the midlatitudes and have very similar temperature and static stability characteristics. The specification of the initial conditions is closely related to the initial dataset derived for baroclinic wave studies with the dynamical cores of general circulation models (GCMs). These are documented in Jablonowski and Williamson (2006a,2006b) and Ullrich *et al.* (2014).

The initial conditions can serve many purposes. They can, for example, be used as a test case during the model development phases, and serve as a debugging tool or for numerical convergence studies. This was our original motivation for their derivation when we used them briefly for the evaluation of the new channel model MCore (Ullrich and Jablonowski, 2012). However, the initial conditions can also serve as the basis for model intercomparisons, or investigations of the impact of the initial state on the baroclinic wave life cycle. The latter is the second focus area of this article. The almost identical f- and β-plane configurations provide an opportunity to compare the different growth rates and most unstable wavelengths of the growing baroclinic waves. We provide

example simulations with the MCore and the Weather and Research Forecasting (WRF) models (Skamarock *et al.*, 2008) and explain the simulation differences via linearized quasi-geostrophic (QG) theory. Of course, the underlying QG theory is well established, and this article does not intend to broaden the theoretical base. Instead, we use the QG framework to validate the model results from a theoretical viewpoint, and demonstrate the close resemblance between the theory and the linear growth phases of the simulations. Having access to a closed-form analytical formulation of the initial conditions eases these QG assessments and closely connects all sections of the article.

The article is organized as follows. Section 2 provides an in-depth description of the initial dataset for our baroclinic wave studies and outlines the generic 'recipe' for the initialization technique. Section 3 specifies the recommended model configuration, briefly introduces the models MCore and WRF, and presents some example simulations on both the f- and β-planes. Section 4 shows how linearized QG theory can be used to validate the simulation results. The conclusions are summarized in section 5.

2. Initial conditions for a baroclinic wave in a channel

2.1. Steady-state initial conditions

The initial conditions for 3D baroclinic wave simulations have been designed for dry atmospheric channel models on a Cartesian plane. Both hydrostatic and non-hydrostatic equation sets with a shallow-atmosphere approximation are supported. The analytical formulation is based on a pressure-based vertical coordinate like the pure pressure coordinate p, the pure $\sigma = p/p_s$ coordinate (Phillips, 1957) or the η (hybrid $\sigma - p$) coordinate (Simmons and Burridge, 1981) with $p = A(\eta)p_0 + B(\eta)p_s$ (see detailed discussion in Appendix A). The reference surface pressure needs to be set to $p_0 = 1000$ hPa here. If other reference surface pressures are employed in a model, such as the sometimes used 'standard atmosphere' of 1013.25 hPa, we recommend resetting the p_0 parameter to 1000 hPa to allow for comparisons to other published results. It is paramount that the initially constant surface pressure p_s is set to the same value $p_s = p_0$. This guarantees that the initial η surfaces coincide with constant σ or pressure surfaces. If other σ systems like $\sigma = (p - p_{top})/(p_s - p_{top})$ are used (Kasahara, 1974), the chosen pressure p_{top} at the top model interface should be set to zero.

In general, the choice of the vertical coordinate system is model-dependent and therefore left to the modelling group, despite the fact that each vertical coordinate system implies different boundary conditions in the vertical direction. In essence, the boundary condition needs to ensure that the vertical velocity, as expressed in the transformed vertical coordinate, is zero at both the surface and the uppermost model interface level. In practice, these formulation differences have been found to be insignificant for the evolution of the baroclinic wave over short $15 - 20$-day time periods. Typically, terrain-following σ or η vertical coordinates are used in hydrostatic GCMs or hydrostatic-pressure-based (also known as mass-based; Laprise, 1992) in non-hydrostatic models. In addition, non-hydrostatic models often utilize a height-based vertical coordinate, as further detailed below and in Appendix B.

The initial state is defined by analytical expressions in horizontally Cartesian (x, y, η) coordinates where $x \in [0, L_x]$ indicates the zonal direction, $y \in [0, L_y]$ represents the meridional direction and $\eta = p/p_s \in [0, 1]$ denotes the position in the vertical direction which is unity at the surface and approaches zero at the model top. The channel widths $L_x = 40\,000$ km and length $L_y = 6\,000$ km are selected in our specification which approximately correspond to the circumference of the Earth in the longitudinal x-direction along the Equator and the meridional extent of the Northern Hemisphere in the y-direction. All physical constants and parameters used for the initial data are given in Tables 1 and 2. Modellers are encouraged to select

Table 1. Physical constants used.

Symbol	Description	Value
a	Radius of the Earth	6.371229×10^6 m
c_p	Specific heat capacity of dry air at constant pressure	1004.5 J kg^{-1}K^{-1}
R_d	Gas constant for dry air	287.0 J kg^{-1}K^{-1}
g	Gravity	9.80616 m s^{-2}
Ω	Angular velocity of the Earth	7.292×10^{-5} s^{-1}

Table 2. Parameters used.

Symbol	Description	Value
f_0	f-plane Coriolis parameter	$2\Omega \sin \varphi_0$
b	Non-dimensional vertical width parameter	2
H	Scale height	$= R_d T_s/g$
L_x	Zonal extent of the domain	40 000 km
L_y	Meridional extent of the domain	6 000 km
N_0	Approximate Brunt–Väisälä frequency at position φ_0	0.014 s^{-1}
p_0	Reference surface pressure	1000 hPa
p_{top}	Suggested maximum pressure position of the model top	20 hPa
q_0	Maximum specific humidity amplitude	0.018 kg kg^{-1}
T_0	Reference temperature	288 K
T_s	Approximate vertically averaged temperature at φ_0	260 K
u_0	Reference zonal wind speed	35 m s^{-1}
u_p	Magnitude of the zonal wind perturbation	1 m s^{-1}
L_p	Width parameter for the perturbation	600 km
x_c	Zonal centre position of the perturbation	2000 km
y_c	Meridional centre position of the perturbation	2500 km
y_0	Meridional position of reference latitude	$L_y/2$
z_s	Surface elevation	0 m
z_{top}	Suggested minimum height position of the model top	30 km
β_0	β-plane parameter	$2\Omega \cos \varphi_0/a$
Γ	Lapse rate	0.005 K m^{-1}
δ	Initial divergence	0 s^{-1}
$\Delta x, \Delta y$	Suggested horizontal grid spacing	100 km
Δz	Suggested maximum vertical grid spacing	1 km
Δy_w	Meridional width parameter for the inclusion of moisture	3 200 km
η_w	η-based width parameter for the inclusion of moisture	0.3
Φ_s	Surface geopotential	0 m^2 s^{-2}
φ_0	Reference latitude	$\pi/4 = 45°$N

the same physical constants and parameters to foster model intercomparisons.

The background flow field is comprised of a zonal jet in the northern midlatitudes that is in hydrostatic and geostrophic balance, enforces the thermal wind relationship, and is a steady-state solution to the shallow-atmosphere equation set. The background zonal wind u, as also specified in Ullrich and Jablonowski (2012), is defined as

$$u(x,y,\eta) = -u_0 \, \sin^2 \left(\frac{\pi \, y}{L_y} \right) \, \ln \eta \, \exp \left\{ - \left(\frac{\ln \eta}{b} \right)^2 \right\}$$
$$= -u_0 \, \sin^2 \left(\frac{\pi \, y}{L_y} \right) \, \ln \eta \, \eta^{\frac{-\ln \eta}{b^2}}, \quad (1)$$

which forces the wind to be zero at the surface and along the north and south y-boundaries. In addition, the wind approaches zero near the model top. The non-dimensional vertical width parameter b is set to 2 and the default value of $u_0 = 35$ m s^{-1} is chosen. Note that the parameter u_0 does not indicate the maximum amplitude of the westerly zonal wind. The maximum is lower and lies around 30 m s^{-1} which resembles the zonal-mean time-mean jet speed in the midlatitudinal troposphere. The centre of the zonal jet in the vertical direction is located around $\eta = 0.24$ or $p = 240$ hPa which is close to the observed position of midlatitudinal jets. As mentioned above, the zonal wind at the surface is zero. Therefore, the surface geopotential is constant and set to $\Phi_s = gz_s = 0$ m^2 s^{-2} which prescribes a flat surface elevation of $z_s = 0$ m. The physical constant g denotes the gravity.

The meridional wind v is set to zero. In addition, the vertical velocity w is set to zero for non-hydrostatic set-ups. This flow field is non-divergent ($\delta = 0$ s^{-1}) and even allows the derivation of the analytical initial conditions for models in vorticity-divergence (ζ,δ) form. The background relative vorticity field is given by

$$\zeta(x,y,\eta) = \frac{2 \pi \, u_0}{L_y} \, \sin \left(\frac{\pi \, y}{L_y} \right) \cos \left(\frac{\pi \, y}{L_y} \right)$$
$$\times \ln \eta \, \exp \left\{ - \left(\frac{\ln \eta}{b} \right)^2 \right\}. \quad (2)$$

This leads to the expression for the absolute vorticity

$$\Omega_a(x,y,\eta) = f + \zeta(x,y,\eta), \quad (3)$$

where the Coriolis parameter f can be chosen to either represent a constant f-plane or β-plane. The two formulations are

$$f = f_0, \quad (4)$$
$$f = f_0 + \beta_0 (y - y_0), \quad (5)$$

with the constant Coriolis parameter $f_0 = 2\Omega \sin \varphi_0$ and the meridional variation of the Coriolis parameter $\beta_0 = 2\Omega \cos \varphi_0/a$ at the constant latitude $\varphi_0 = 45°$N. The radius of the Earth is symbolized by a, Ω denotes the Earth's angular velocity and $y_0 = L_y/2$ is the centre point of the domain in the y-direction. The steady-state zonal wind and relative vorticity field with respect to the vertical η coordinate are depicted in Figure 1. They are identical for both the f- and β-plane formulation of the initial dataset.

As the last step, we need expressions for the balanced geopotential and temperature fields. The geopotential is given by

$$\Phi(x,y,\eta) = \langle \Phi(\eta) \rangle + \Phi'(x,y) \ln \eta \, \exp \left\{ - \left(\frac{\ln \eta}{b} \right)^2 \right\} \quad (6)$$

with the horizontal-mean geopotential

$$\langle \Phi(\eta) \rangle = \frac{T_0 \, g}{\Gamma} \left(1 - \eta^{\frac{R_d \Gamma}{g}} \right) \quad (7)$$

and the horizontal variation

$$\Phi'(x,y) = \frac{u_0}{2} \left[(f_0 - \beta_0 y_0) \left\{ y - \frac{L_y}{2} - \frac{L_y}{2 \pi} \sin \left(\frac{2\pi y}{L_y} \right) \right\} \right.$$
$$+ \frac{\beta_0}{2} \left\{ y^2 - \frac{L_y y}{\pi} \sin \left(\frac{2\pi y}{L_y} \right) \right.$$
$$\left. - \frac{L_y^2}{2 \pi^2} \cos \left(\frac{2\pi y}{L_y} \right) - \frac{L_y^2}{3} - \frac{L_y^2}{2 \pi^2} \right\} \right]. \quad (8)$$

The reference temperature T_0, the lapse rate Γ and the gas constant for dry air R_d are set as in Tables 1 and 2. The corresponding temperature distribution comprises the level-dependent horizontal-mean temperature $\langle T(\eta) \rangle$ and a horizontal temperature perturbation T'. They are given by

$$T(x,y,\eta) = \langle T(\eta) \rangle$$
$$+ \frac{\Phi'(x,y)}{R_d} \left\{ \frac{2}{b^2} (\ln \eta)^2 - 1 \right\} \exp \left\{ - \left(\frac{\ln \eta}{b} \right)^2 \right\} \quad (9)$$

with the horizontal-mean temperature

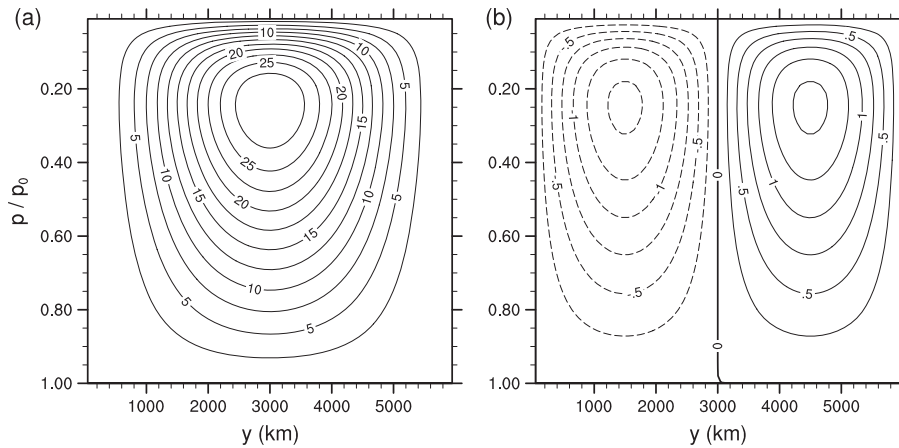$$\langle T(\eta) \rangle = T_0 \, \eta^{\frac{R_d \Gamma}{g}}. \quad (10)$$

Figure 1. Meridional–vertical cross-sections of the initial steady-state (a) zonal wind (m s^{-1}) and (b) relative vorticity (10^{-5} s^{-1}) with respect to the η vertical coordinate. Negative contours are dashed.

This horizontal-mean temperature profile describes a linear temperature decrease with height, using a lapse rate of Γ. As mentioned above, the initial data enforce hydrostatic, geostrophic and thermal wind balance analytically. If a constant f-plane is desired, the parameter β_0 can simply be set to zero which simplifies the initial conditions.

The initial temperature, geopotential height, potential temperature, absolute vorticity, Brunt–Väisälä frequency N and Ertel's PV on the constant f-plane are shown in Figure 2. The corresponding initial data on the β-plane are presented in Figure 3. Both plots depict the initial state with respect to the vertical η coordinate. The potential temperature patterns and N indicate that the initial data are statically stable. In addition, the absolute vorticity and PV distributions (positive on this Northern Hemispheric plane) fulfill the conditions for inertial and symmetric stability. However, the profiles are unstable with respect to barotropic and baroclinic instability mechanisms. Figure 3 demonstrates that the addition of the β-plane leads to only minor changes of the initial temperature and geopotential fields, and has very similar static stability characteristics. The geopotential equation (6) is needed for 3D channel models with height-based vertical coordinates. Then an accurate root-finding algorithm is recommended to determine the corresponding η-level for any desired height position z. This iterative method, which is also applicable to isentropic vertical coordinates (Jablonowski and Williamson, 2006a), is outlined in Appendix B. The Supplement also shows the corresponding initial data with respect to the z coordinate. The latter two figures depict the meridional–vertical cross-section of the pressure field instead of the geopotential height. Furthermore, Appendix B lists the pressure, density and potential temperature equations that are typically needed for non-hydrostatic models.

In general, the complexity of the initial conditions can easily be extended to allow for a wide range of application areas. For example, the background zonal wind profile used here could be overlaid with a meridional zonal wind gradient to introduce either cyclonic or anticyclonic barotropic wind shear. Such modifications will impact the baroclinic wave life cycles as discussed by e.g. Davies *et al.* (1991), Thorncroft *et al.* (1993) or Davis (2010). Therefore, the description of the analytical initial state presented here can also be viewed as a generic recipe. This recipe closely follows the technique that was outlined for spherical geometry in the appendix of Jablonowski and Williamson (2006b). Once a zonally symmetric background zonal wind field is analytically specified, and $v = w = 0$ m s^{-1} and $p_s = p_0$ are selected, the steady-state meridional momentum equation (written for a vertical pressure coordinate) can be integrated to yield the horizontal geopotential perturbation Φ'. The integration constant follows from the condition that the horizontal mean of Φ' must vanish. Utilizing the hydrostatic balance then gives the horizontal temperature perturbation T'. All that is left is

the selection of the horizontal-mean background stratification $\langle T(\eta) \rangle$, which then yields the balanced mean geopotential $\langle \Phi(\eta) \rangle$ via the integration of the hydrostatic equation. The corresponding integration constant must ensure that the horizontal-mean $\langle \Phi_s(\eta) \rangle$ at the surface is zero. As a last step, the static stability of the new initial data needs to be assessed to guarantee that the chosen design and parameters lead to a statically stable configuration. If necessary, parameters like u_0 might need to be adjusted to yield $N^2 > 0$ s^{-2}. Note that a non-zero zonal wind at the surface will lead to a non-zero surface geopotential Φ_s and thereby a meridional variation of the surface elevation z_s.

These initial conditions are perfectly balanced in a continuous sense, and very well balanced in the discrete system. If an even better discrete balance is desired, e.g. volume-mean values for finite-volume models, then Gaussian quadrature can be used to subsample the initial fields at the Gaussian quadrature points.

The initial conditions can also be easily extended to allow for simulations of idealized moist baroclinic waves as investigated by e.g. Tan *et al.* (2004), Waite and Snyder (2013) or Mirzaei *et al.* (2014). As before, none of these authors specify analytical conditions for their initial moisture fields. In addition, their prescribed initial relative humidity fields differ, and the balancing algorithms for the moist conditions are not thoroughly described. Appendix C provides the details of an analytical technique that adds specific humidity to the balanced initial fields.

2.2. Baroclinic wave triggering mechanism

A baroclinic wave can be triggered if the balanced zonal wind is overlaid with a localized perturbation. Here a zonal wind perturbation u' with a Gaussian profile is centred at $(x_c, y_c) = (2000 \text{ km}, 2500 \text{ km})$ and given by

$$u'(x, y, \eta) = u_p \exp\left\{ -\left(\frac{(x - x_c)^2 + (y - y_c)^2}{L_p^2} \right) \right\} \quad (11)$$

with the width parameter $L_p = 600$ km and maximum amplitude $u_p = 1$ m s^{-1}. This perturbation is not balanced by the mean state and gets superimposed on the zonal wind field (1) by adding u' to u at each grid point at all model levels:

$$u_{\text{wave}}(x, y, \eta) = u(x, y, \eta) + u'(x, y, \eta). \quad (12)$$

The zonal wind perturbation is depicted in Figure 4. It covers a domain with a diameter of about 2500 km. As an aside, the unbalanced perturbation initially triggers high-speed gravity waves. They are apparent during the early stages and are damped by diffusion over time before the growth of the baroclinic wave dominates the fluid flow.
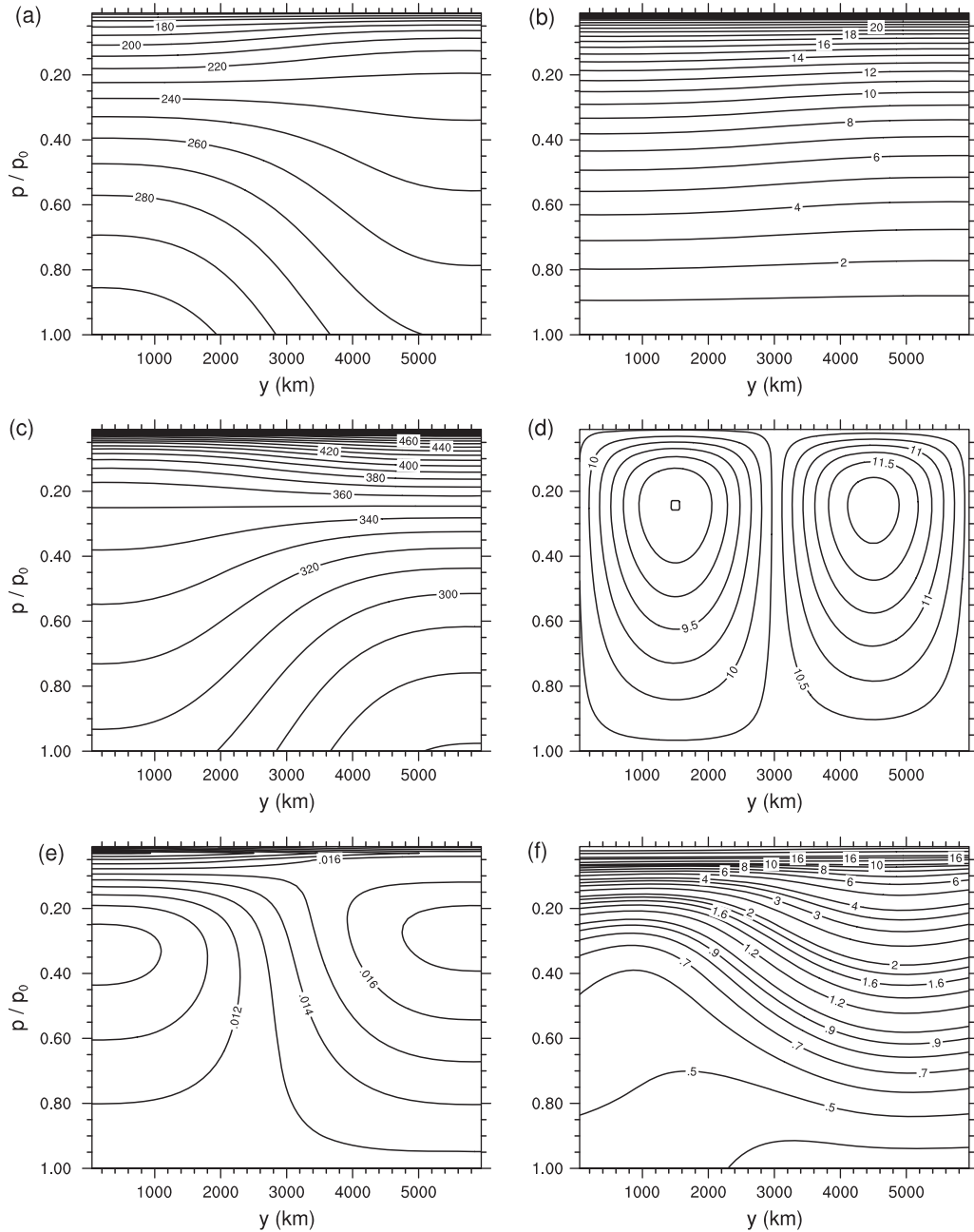
Figure 2. Meridional–vertical (η) cross-sections of the steady-state initial conditions on a constant f-plane: (a) temperature (K), (b) geopotential height (km), (c) potential temperature (K), (d) absolute vorticity (10^{-5} s^{-1}), (e) Brunt–Väisälä frequency N (s^{-1} and (f) Ertel's PV (PVU = 10^{-6} K m^2 kg^{-1} s^{-1}).

If models employ the relative vorticity and divergence as prognostic variables, the corresponding perturbations are given by

$$\zeta'(x, y, \eta) = \frac{2(y - y_c) u'}{L_p^2}, \qquad (13)$$

$$\delta'(x, y, \eta) = \frac{-2(x - x_c) u'}{L_p^2}. \qquad (14)$$

These then need to be added to the background ζ and δ fields.

2.3. Boundary conditions for channel models

Periodic boundary conditions are suggested for the x-direction. If such periodic conditions are not possible due to the model design, the analytical initial state can be prescribed along the x-boundaries as long as the developing baroclinic wave does not approach the easternmost edge of the domain. This is not the case for short 15-day simulations when using the suggested parameter set with $u_0 = 35$ m s^{-1}. In case boundary issues arise, the use of a zonal damping layer could be considered. Note that the channel

width L_x can also be varied, even decreased, as long as the wave does not approach the x-edge. This does not change the character of the solution.

At the southern boundary $y = 0$ and northern boundary $y = L_y$, additional boundary conditions must be specified. Either no-flux or prescribed Dirichlet boundary conditions can be used, and either choice produces indistinguishable results. The following time-invariant Dirichlet boundary conditions in the y-direction have been used here:

$$p_s(x, y = 0, t) = p_s(x, y = L_y, t) = p_0, \qquad (15)$$

$$u(x, y = 0, \eta, t) = u(x, y = L_y, \eta, t) = 0, \qquad (16)$$

$$v(x, y = 0, \eta, t) = v(x, y = L_y, \eta, t) = 0, \qquad (17)$$

$$w(x, y = 0, \eta, t) = w(x, y = L_y, \eta, t) = 0, \qquad (18)$$

$$T(x, y = 0, \eta, t) = T(x, y = 0, \eta, t = 0), \qquad (19)$$

$$T(x, y = L_y, \eta, t) = T(x, y = L_y, \eta, t = 0). \qquad (20)$$

This formulation effectively prescribes the initial state along the y-boundaries. If the potential temperature Θ is used as the prognostic variable, the temperature boundary condition can
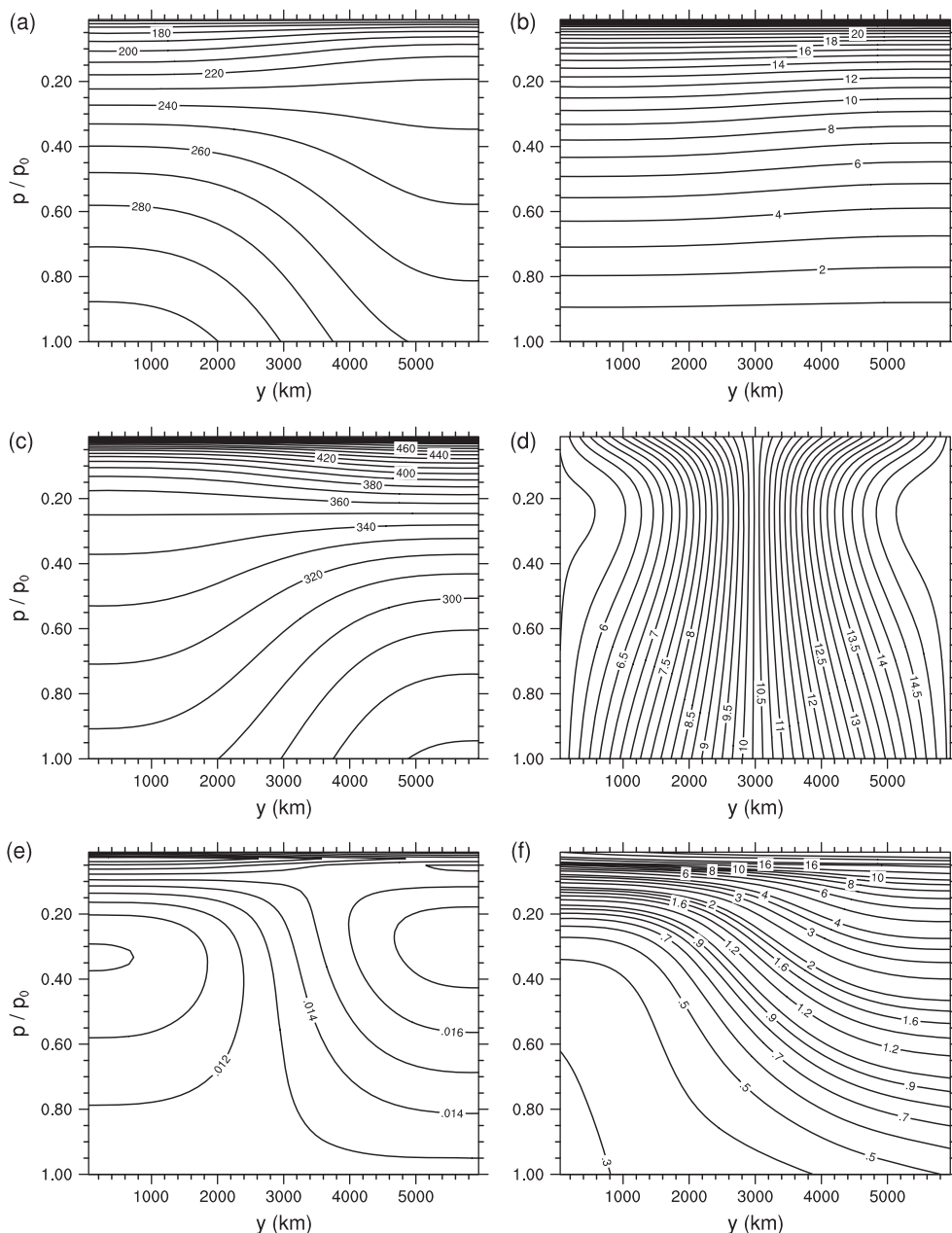
(a)

(b)

(c)

(d)

(e)

(f)

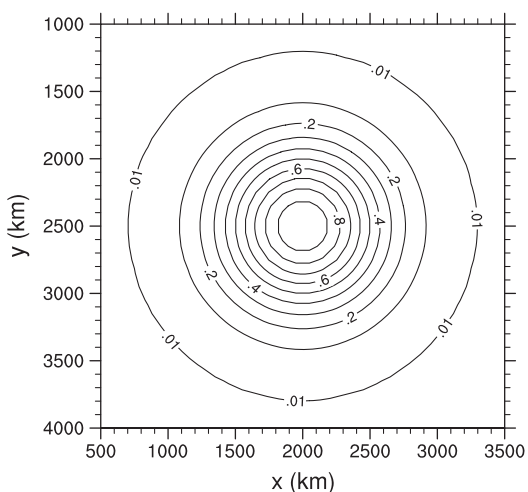**Figure 3.** As Figure 2, but on the β-plane.

Figure 4. The vertically uniform zonal wind perturbation (m s^{-1}).

simply be converted to Θ. If boundary conditions are needed for the pressure p or density ρ, they are expressed in the same way as the boundary conditions for T. In our experiments we

have not observed any negative boundary effects at the $y = 0$ or $y = L_y$ edges of the domain over the 15-day simulation period and recommend not using any sponge zones near the y-edges.

3. Selected configurations and numerical results

3.1. Flow and model configurations

The initial data can be used for numerical or physical science questions, both on a constant f- and β-plane. If the initial data are used as a test case e.g. to support the intercomparison of numerical schemes or to serve as a debugging tool during the model development phases, we recommend using the steady-state initial conditions without the zonal wind perturbation as the first step. This assesses how well and how long the numerical discretization can maintain the initial steady state which is the analytical solution. If possible the model should be run without explicit diffusion to minimize the degradation of the steady state. The second more advanced configuration evaluates the evolution of a baroclinic wave in the Northern Hemisphere. It is triggered when using the steady-state initial conditions with the overlaid zonal wind perturbation. If applicable and needed, the model- and resolution-dependent subgrid-scale diffusion mechanisms

with standard parameters should be used. All simulations should cover at least a 15-day time period.

If numerical convergence-with-resolution studies are desired, we recommend using the horizontal grid spacings $\Delta x = \Delta y = 200, 100, 50$ and 25 km. If physical science questions are addressed, such as the impact of the varying Coriolis force on the evolution of a baroclinic wave, as is the focus in this article, the horizontal grid spacing should be at least 100 km or finer. At this grid spacing, solutions start to converge.

In the vertical direction, at least 30 levels with a suggested maximum grid spacing $\Delta z = 1$ km should be used. The model top should lie at or above the $p_{top} = 20$ hPa or $z_{top} = 30$ km position to capture the majority of the zonal jet structure in the upper atmosphere. A higher-altitude model top is even preferred, but adds extra computational cost. The type of vertical coordinate and the placement of the vertical levels should be documented. In addition, we recommend listing the time steps, dissipation mechanisms and their coefficients for all simulations to allow for straightforward comparisons with other published results. The baroclinic instability wave does not have an analytical solution. Therefore, high-resolution ($\Delta x = \Delta y \leq 25$ km) reference solutions and their uncertainties need to be assessed for convergence studies. These suggestions closely follow the recommendations for the baroclinic wave test case in spherical geometry documented in Jablonowski and Williamson (2006a).

3.2. Example models

We pick two non-hydrostatic models to demonstrate the characteristics of the baroclinic wave. Both models produce comparable evolutions of the baroclinic instability, and therefore give confidence that our solutions are credible. In addition, this provides two points of comparison for other modellers. Since this is not the focus of this article, we do not conduct a thorough model intercomparison. Instead, we use these example results to draw attention to the interesting evolution paths of the baroclinic instability depending on the f- and β-plane approximations. This further motivates our theoretical investigations in section 4.

The two example models are the channel configuration of MCore (Ullrich and Jablonowski, 2012) and WRF, version 3, described in Skamarock *et al.* (2008). The latter has been developed at the National Center for Atmospheric Research (NCAR). In brief, both models use a finite-volume discretization and either a vertically implicit (MCore) or split-explicit (WRF) time-split approach for handling the high-speed waves in the vertical direction. MCore utilizes a fourth-order spatial discretization on an unstaggered A-grid, whereas WRF's numerical scheme is second-order accurate and built upon a staggered C-grid. MCore employs a height-based vertical coordinate, whereas WRF is designed with the hydrostatic-pressure (mass-based) vertical coordinate. All experiments use identical horizontal grid spacings of $\Delta x = \Delta y = 100$ km. MCore is configured with 30 vertical levels which utilize an equidistant vertical grid spacing of $\Delta z = 1$ km (with the lowermost full model level position at $z = 500$ m) and a model top at $z_{top} = 30$ km. WRF is configured with 64 vertical levels with non-equidistant vertical grid spacings which are $\Delta z \approx 300$ m close to the ground (with the lowermost full model level position at $z \approx 150$ m). The spacing is stretched in the vertical direction, with the same model top at 30 km. The MCore time step is $\Delta t = 240$ s, and WRF uses a time step of 600 s. MCore's diffusion mechanism is a flow-dependent implicit numerical diffusion which is part of its Riemann solver as explained in Ullrich and Jablonowski (2012). WRF's diffusion mechanisms are 3D divergence damping, an external mode filter and a time-off-centring technique for sound waves, which all use the standard coefficients documented in Skamarock *et al.* (2008). No Laplacian-type explicit diffusion or hyper-diffusion mechanisms are applied.

3.3. Snapshots of the baroclinic wave on the f- and β-plane

This section focuses on selected snapshots of the baroclinic wave on the f- and β-plane. Example results for the steady-state configuration, and how it can be used for the assessment of the order of accuracy of a numerical scheme, are shown in Ullrich and Jablonowski (2012) which numerically confirmed the theoretical fourth-order accuracy of the model MCore. We run the baroclinic wave simulations for 15 days to capture the initial and rapid development stages of the baroclinic disturbance. In general, the baroclinic wave starts growing noticeably after ≈ 6 days and evolves rapidly afterwards. Once the wave breaks, the flow enters a turbulent mixing stage.

Figures 5 and 6 display snapshots of the baroclinic waves simulated on the f- and β-plane, respectively, with $u_0 = 35$ m s^{-1}. The β-plane formulation adds extra complexity to the simulation and gives insight into the effects of a varying Coriolis force. In particular, Figure 5 shows the (a–c) WRF and (d–f) MCore f-plane 500 m pressure, temperature and relative vorticity at day 12. This vertical position is identical to the lowest model level in MCore, and requires vertical interpolations of the WRF data. The 500 m low-lying position is chosen since the baroclinic wave develops its strongest gradients close to the ground. Figure 6 shows the identical 500 m fields at day 10 as simulated with the β-plane variant of the initial conditions in (a–c) WRF and (d–f) MCore. The baroclinic waves, although idealized, represent very realistic flow features in both Coriolis-term configurations and models. Strong temperature fronts develop which are associated with the evolving sequence of low and high pressure systems. The latter are also mirrored in the relative vorticity patterns with strong positive relative vorticity near the low pressure centres. The WRF and MCore results closely resemble each other, suggesting that the flow patterns are trustworthy.

The growth rate of the wave strongly depends on the choice of the f- or β-plane approximation and the u_0 parameter. In our experiments, the 500 m temperature wave breaks around day 13.5 on the f-plane. In contrast, the 500 m temperature wave evolves more rapidly on the β-plane and breaks around day 11. In addition, the β-plane solution is confined to a narrower meridional width and exhibits a shorter wavelength of about 3300 km. The estimated wavelength of the f-plane simulation is about 4000 km. As an aside, if an alternative parameter $u_0 = 45$ m s^{-1} is utilized, the atmosphere becomes even more baroclinic with increased vertical wind shear, and the evolution of the wave speeds up by about two days in both cases. We note that the MCore relative vorticity plots in Figures 5(f) and 6(f) correct the relative vorticity plots shown in Ullrich and Jablonowski (2012) (their Figures 12(c) and 13(c)) whose relative vorticity magnitudes were a factor of two too large.

Zonal–vertical cross-sections of the flow from the MCore channel model at the location $y = L_y/2$ are shown in Figure 7 for the f-plane at day 12 and in Figure 8 for the β-plane at day 10. The figures depict the deviations of the geopotential, temperature, zonal velocity and meridional velocity from the balanced initial state which we define as 'perturbations'. Both the f- and β-plane geopotential perturbation and meridional wind show strong westward tilts with height. The temperature perturbations tilt eastward with height, especially in the lower atmosphere.

Note that the Froude numbers $Fr_h = U/(LN) \approx 2 \times 10^{-4}$ in the horizontal and $Fr_z = U/(H_dN) \approx 0.071$ in the vertical, as well as the Rossby number $Ro = U/(Lf_0) = 0.025$, of the flow are small ($\ll 1$) and thereby lie in the asymptotic regime of the QG theory. These assessments utilize the characteristic horizontal velocity-scale of $U = 10$ m s^{-1}, the horizontal length-scale of $L = 4000$ km of the baroclinic waves, the vertical depth-scale of $H_d = 10$ km, the Brunt–Väisälä frequency $N = 0.014$ s^{-1}, and the Coriolis parameter $f_0 \approx 10^{-4}$s^{-1} at 45°N. It means that the atmosphere is highly stratified and dominated by rotational effects which essentially confines the fluid to horizontal motions (Waite
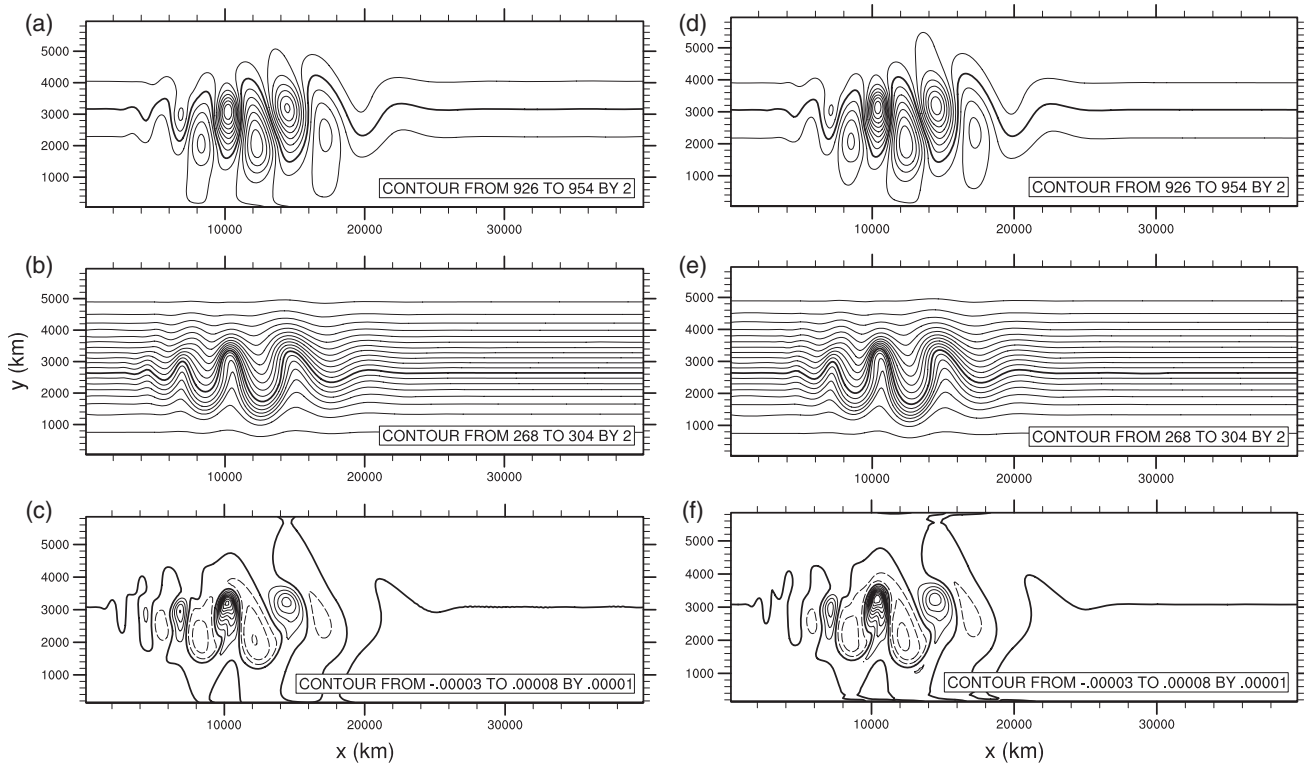
Figure 5. Horizontal x–y cross-sections of the baroclinic wave at day 12 on the f-plane as simulated by the (a–c) WRF and (d–f) MCore channel model. The plots show the (a,d) 500 m pressure field (hPa) with enhanced 942 hPa contour line, (b,e) 500 m temperature (K) with the lowest temperatures near $y = 0$ km and enhanced 290 K contour, and (c,f) 500 m relative vorticity (s^{-1}) with enhanced zero contour.
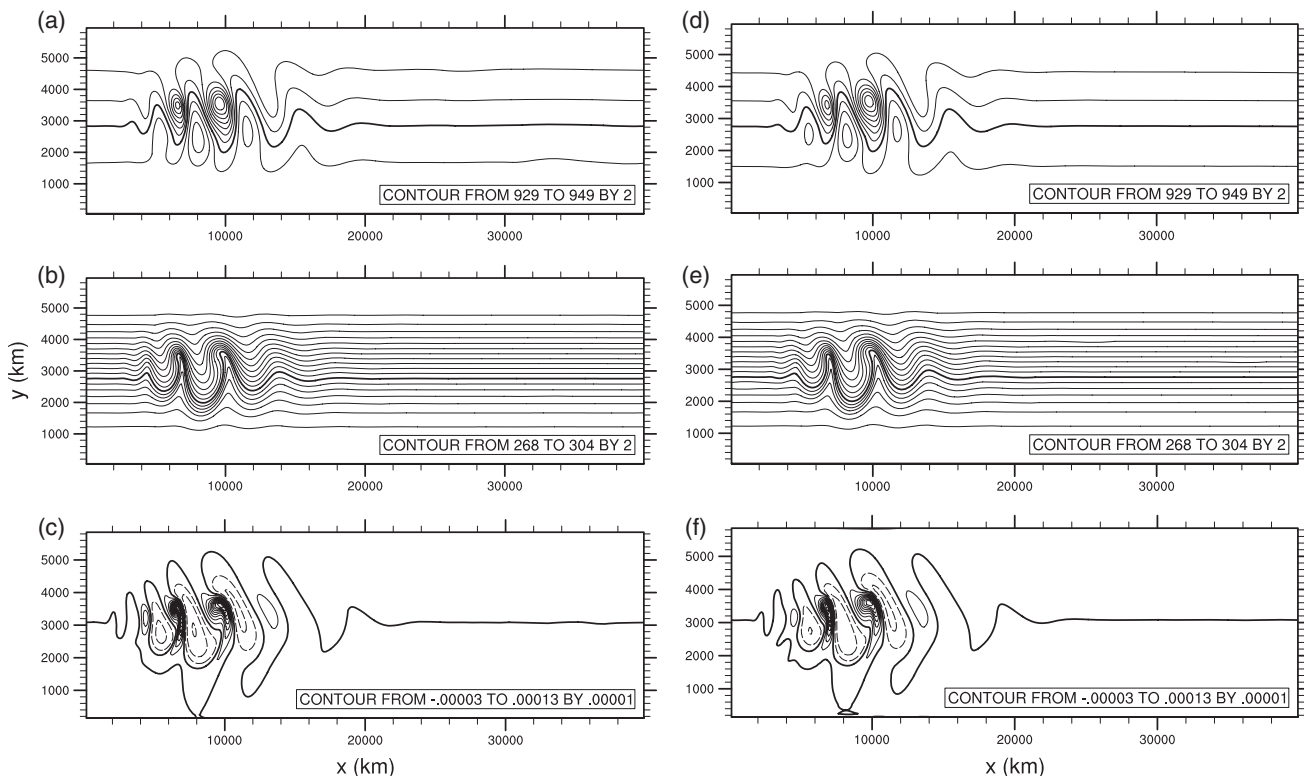

Figure 6. As Figure 5, but for day 10 on the β-plane. In (a,d) the enhanced contour line is at 943 hPa.

and Bartello, 2006). This provides motivation to use theoretical concepts, like the linearized QG theory, for further analysis and validation of the results in the next section. The remainder of the article utilizes QG theory and the model MCore to analyze the differences between the f- and β-plane simulations.

4. Analysis

The dynamical behaviour of the baroclinic instability is well understood in the context of linearized QG theory. The linear theory is valid only until the wave breaks, when nonlinearities in the flow lead to mixing between wave modes. In this section we apply the known theory for the baroclinic instability to the flow configurations proposed in sections 2 and 3.1.

4.1. The baroclinic instability in a continuously stratified atmosphere

In order to analyze the evolution of the baroclinic instability we apply QG theory e.g. as detailed in Holton (2004). Here, we briefly
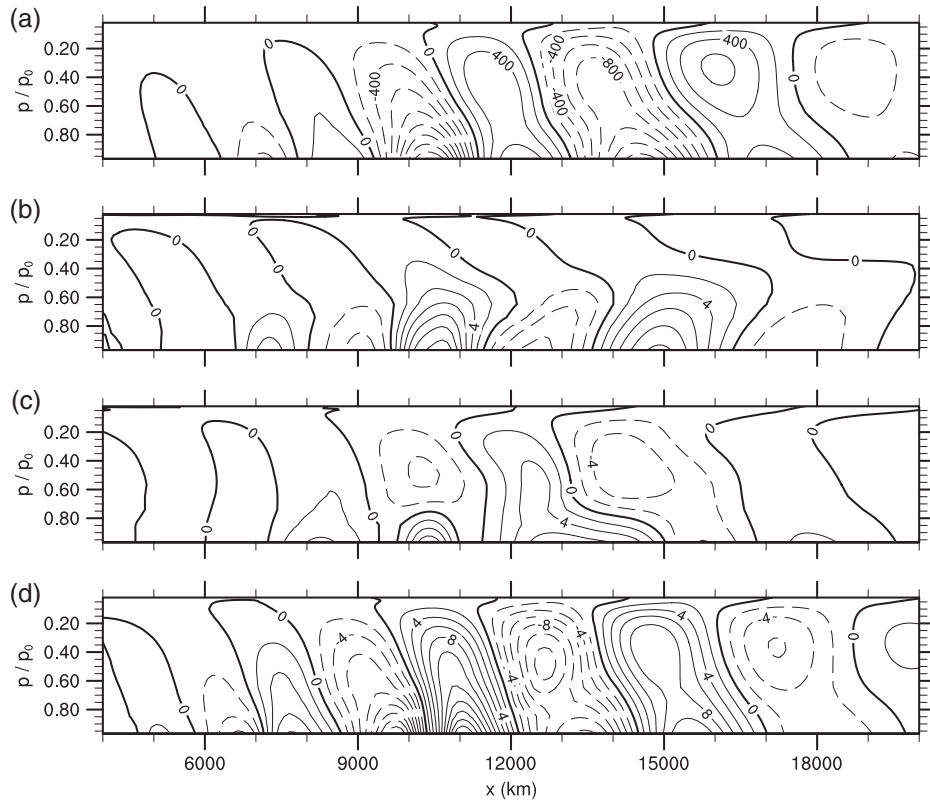
Figure 7. Zonal–vertical cross-sections through $y = L_y/2$ of the baroclinic wave at day 12 on the f-plane as simulated by the MCore channel model. The plots show (a) geopotential (Φ) perturbation, (b) temperature perturbation, (c) zonal velocity perturbation and (d) meridional velocity. The contour spacing is (a) 200 m² s⁻², (b) 2 K, (c) 2 m s⁻¹ and (d) 2 m s⁻¹. Dashed lines denote negative contours, and the zero contour is enhanced.
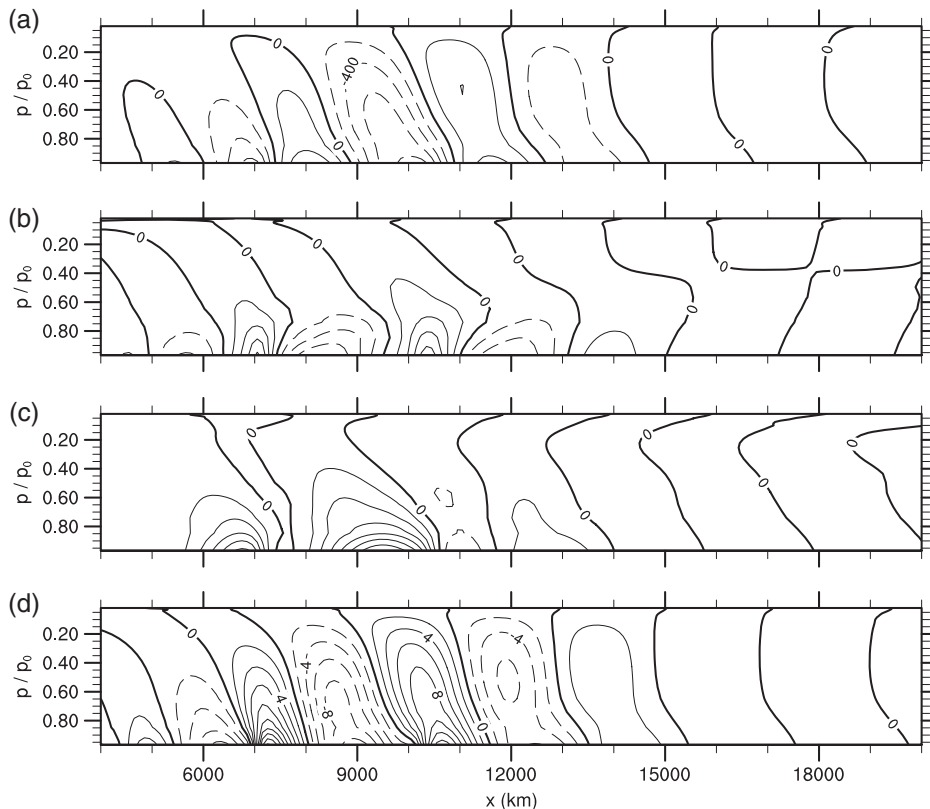

Figure 8. As Figure 7, but for day 10 on the β-plane.

summarize the most important QG aspects as they apply to our analyses of the f-plane and β-plane solutions. The linear QG theory typically utilizes log-pressure height coordinates, which are defined as

$$z^* = -H \ln \left(\frac{p}{p_0} \right),$$ (21)

where $p_0 = 1000$ hPa is the reference surface pressure, $H = R_d T_s/g$ is a standard scale height and T_s is an approximate vertically averaged temperature at position $y_0 = 0.5 L_y$, chosen to be 260 K. The log-pressure height is roughly equivalent to a geometric height in the troposphere, although these profiles can diverge significantly in regions where the temperature does not match T_s. To analyze the stability of the baroclinic instability we

define a geostrophic streamfunction

$$\psi \equiv \Phi/f_0, \tag{22}$$

so that the geostrophic wind can be expressed as $\mathbf{v}_\psi = \mathbf{k} \times \nabla \psi$. We further utilize the QG PV q, defined in log-pressure coordinates as

$$q \equiv \nabla^2 \psi + f + \frac{1}{\rho_0} \frac{\partial}{\partial z^*} \left(\frac{f_0^2 \rho_0}{N^2} \frac{\partial \psi}{\partial z^*} \right). \tag{23}$$

Here, $\rho_0(z^*)$ is an approximate background density profile which is obtained analytically at the meridional centre y_0 of the domain,

$$\rho_0(z^*) = \frac{p(z^*)}{R_d \, T \left\{ 0, \frac{L_y}{2}, \eta(z^*) \right\}}, \tag{24}$$

using the temperature profile (9). The QG PV equation and the thermodynamic equation (for an adiabatic flow) can then be expressed in log-pressure coordinates as

$$\left(\frac{\partial}{\partial t} + \mathbf{v}_\psi \cdot \nabla \right) q = 0, \tag{25}$$

and

$$\left(\frac{\partial}{\partial t} + \mathbf{v}_\psi \cdot \nabla \right) \frac{\partial \Phi}{\partial z^*} + w^* N^2 = 0, \tag{26}$$

respectively. Here $w^* = Dz^*/Dt$ is the vertical velocity in log-pressure coordinates and t is time.

The governing equations (25) and (26) are linearized using

$$q(x, y, z^*, t) = \overline{q}(y, z^*) + q'(x, y, z^*, t), \tag{27}$$

$$\psi(x, y, z^*, t) = \overline{\psi}(y, z^*) + \psi'(x, y, z^*, t), \tag{28}$$

where the overline denotes a zonally and time-averaged mean state, and the prime symbolizes the deviations from the mean basic state. This leads to the linearized potential vorticity equation

$$\left(\frac{\partial}{\partial t} + \overline{u} \frac{\partial}{\partial x} \right) q' + \frac{\partial \overline{q}}{\partial y} \frac{\partial \psi'}{\partial x} = 0, \tag{29}$$

with

$$q' = \nabla^2 \psi' + \frac{1}{\rho_0} \frac{\partial}{\partial z^*} \left(\frac{f_0^2 \rho_0}{N_0^2} \frac{\partial \psi'}{\partial z^*} \right) \tag{30}$$

and

$$\frac{\partial \overline{q}}{\partial y} = \beta - \frac{\partial^2 \overline{u}}{\partial y^2} - \frac{1}{\rho_0} \frac{\partial}{\partial z^*} \left(\frac{f_0^2 \rho_0}{N_0^2} \frac{\partial \overline{u}}{\partial z^*} \right). \tag{31}$$

The constant Brunt–Väisälä frequency $N_0 = 0.014 \, \text{s}^{-1}$ represents an average near the meridional centre y_0 in the region of greatest instability which lies between the surface and $\eta \approx 0.25$ (see also Figures 2(e) and 3(e)). The balanced initial condition for u (1) serves as the mean background wind $\overline{u}(y, z^*)$.

The linearized thermodynamic equation (26) is applied at the top and bottom boundaries of the domain (the top boundary is assumed to be a rigid lid) where $w^* = 0$, so that it takes the form

$$\left(\frac{\partial}{\partial t} + \overline{u} \frac{\partial}{\partial x} \right) \frac{\partial \psi'}{\partial z^*} - \frac{\partial \psi'}{\partial x} \frac{\partial \overline{u}}{\partial z^*} = 0. \tag{32}$$

No-flux boundary conditions are applied at the meridional edges of the domain, which leads to the additional condition

$$\frac{\partial \psi'}{\partial x} = 0 \quad \Longrightarrow \quad \psi' = 0, \quad \text{at } y = 0 \text{ and } y = L_y. \tag{33}$$

The perturbation streamfunction is assumed to consist of a single zonal Fourier component propagating zonally

$$\psi'(x, y, z^*, t) = \text{Re} \left[\Psi(y, z^*) \exp \{ik(x - ct)\} \right], \tag{34}$$

where Re denotes the real part of the equation, $\Psi = \Psi_r + i\Psi_i$ is the complex amplitude function, $c = c_r + ic_i$ is the complex phase speed, i symbolizes the imaginary unit, and k is the zonal wave number

$$k = \frac{2\pi \widetilde{k}}{L_x}, \tag{35}$$

with the non-negative integer $\widetilde{k} \in \{0, 1, 2, \dots\}$. It denotes the number of cycles of the Fourier mode over the zonal domain. It then follows from (29) and (34) that

$$(\overline{u} - c) \left\{ \frac{\partial^2 \Psi}{\partial y^2} - k^2 \Psi + \frac{1}{\rho_0} \frac{\partial}{\partial z^*} \left(\frac{f_0^2 \rho_0}{N^2} \frac{\partial \Psi}{\partial z^*} \right) \right\} + \frac{\partial \overline{q}}{\partial y} \Psi = 0, \tag{36}$$

which is an elliptic partial differential equation for Ψ in $(y, z) \in [0, L_y] \times [0, z^*_{\text{top}}]$. Boundary conditions in the meridional direction are given by (33), and at $z = 0, z^*_{\text{top}}$ by (32) and (34),

$$(\overline{u} - c) \frac{\partial \Psi}{\partial z^*} - \frac{\partial \overline{u}}{\partial z^*} \Psi = 0. \tag{37}$$

Since the phase speed c is unknown, we must solve a Sturm–Liouville (or boundary-value) problem to find non-trivial solutions of (36) and (37) for eigenvalue/eigenfunction pairs $(c, \Psi(y, z^*))$.

Analytical solutions of the boundary-value problem are difficult or impossible to obtain in general, and consequently we rely on a numerical solution. Our numerical approach is described in detail in Appendix D. To quickly summarize, we discretize (36) and (37) using standard second-order finite-difference operators, so that the Sturm–Liouville problem can be rewritten as an eigenvalue problem of the form

$$\mathbf{F}(k) \boldsymbol{\Psi}_d = c \boldsymbol{\Psi}_d, \tag{38}$$

where $\boldsymbol{\Psi}_d$ is a vectorized approximation to Ψ at each of the mesh nodes and $\mathbf{F}(k)$ is a discrete matrix operator which is dependent on the horizontal wave number. The resulting eigenvalue problem is then solved using the `eig` command in Matlab, which yields all discrete pairs $(c, \boldsymbol{\Psi}_d)$ that satisfy (38).

4.2. Most unstable modes

The non-trivial wave solutions (34) of the boundary-value problem can also be expressed in the form

$$\psi'(x, y, z^*, t) = \exp(kc_i t) \, \text{Re} \left[\Psi(y, z^*) \exp\{ik(x - c_r t)\} \right] \tag{39}$$

$$= \exp(kc_i t) \, \Psi_r \cos \{k(x - c_r t)\}$$
$$- \exp(kc_i t) \, \Psi_i \sin \{k(x - c_r t)\} . \tag{40}$$

Consequently, solutions with positive imaginary component $c_i > 0$ will cause the baroclinic instability to intensify over time.

The streamfunction wave mode with maximum growth rate $\alpha = kc_i$ will become dominant as $t \to \infty$, and so is referred to as the *most unstable wave mode*. In Figure 9 we plot the zonal phase speed c_r and growth rate kc_i for the discrete wave number range $\widetilde{k}$ between 0 and 20. Figure 9(b) shows that the most unstable modes (the maxima) as derived via QG theory occur at the discrete wave number $\widetilde{k} = 10$ on the f-plane, with $kc_i \approx 6.59 \times 10^{-6} \, \text{s}^{-1}$, and at $\widetilde{k} = 12$ on the β-plane, with $kc_i \approx 7.21 \times 10^{-6} \text{s}^{-1}$. This corresponds to a wavelength of roughly 4000 km on the f-plane and 3333 km on the β-plane. As displayed in Figure 9(a), the zonal phase speed of this mode is $11.43 \, \text{m s}^{-1}$ on the f-plane and
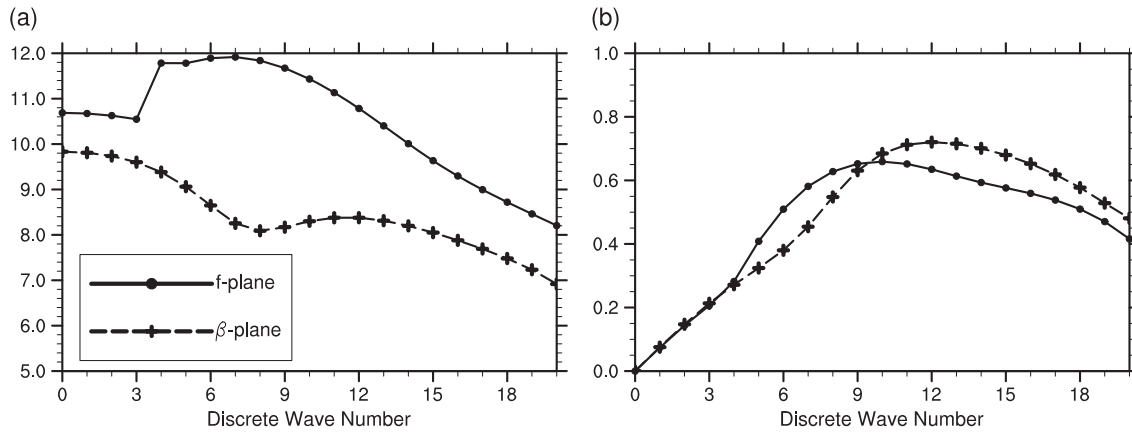
(a)

(b)

Figure 9. (a) Real phase speed c_r (m s^{-1}) and (b) growth rate kc_i (10^{-5} s^{-1}) of the streamfunction wave from QG theory for the discrete wave number range $\widetilde{k}$ between 0 and 20.

8.38 m s^{-1} on the β-plane, which is significantly slower than the maximum zonal background flow $\overline{u}$ with ≈ 30 m s^{-1} in the upper atmosphere.

Besides the most unstable wave modes $\widetilde{k} = 10$ (f-plane) and $\widetilde{k} = 12$ (β-plane) displayed in Figure 9(b), there are also neighbouring wave numbers that grow at comparable rates. On the f-plane these range from wave numbers 8 to 12, and on the β-plane these range from wave numbers 10 to 14. This aspect can lead to sensitivities in numerical solutions when asymmetric meshes are used, such as triangular or hexagonal grids. For example, the barotropic instability wave test case by Galewsky *et al.* (2004) exposes such sensitivities in the 2D shallow-water framework. Wave modes with similar growth rates were found to be impacted by grid inhomogeneities, especially at low resolutions with grid spacings > 120 km, which can lead to rather different evolutions of the growing instability wave. Examples are displayed in e.g. St-Cyr *et al.* (2008) and Weller *et al.* (2012), who showed that the growth of the Galewsky *et al.* (2004) barotropic instability wave on the sphere can be overshadowed by the growth of numerical discretization errors that originate from non-Cartesian grids. Evaluating such potential grid imprinting signatures in 3D channel models is therefore another application area of the initial conditions presented here.

We highlight that the QG growth rate of the most unstable mode on the β-plane is significantly larger than the growth rate on the f-plane. The higher growth rate and the shorter wavelength on the β-plane confirm our numerical findings from section 3.3. Interestingly, this QG result derived via the continuous equations seem to be partly contrary to results from the two-layer QG baroclinic wave theory (e.g. section 8.2 of Holton, 2004), which hold that the addition of a β term introduces a stabilizing effect to a baroclinic instability. However, we do note that the theoretical growth rate from the β-plane is smaller for longer waves ($\widetilde{k} < 10$) in agreement with the two-layer theory.

In Figure 10 we plot the meridional–vertical cross-sections of the real and imaginary components of the amplitude function Ψ for the most unstable wave modes on the f- and β-plane. Equation (40) explains how the real Ψ_r and imaginary Ψ_i components impact the pattern of the baroclinic wave. Their relative magnitudes determine the phase of the wave for any position (y, z^*).

Some example wave perturbations are shown in Figures 11 and 12. The figures depict the zonal–vertical cross-sections of the geopotential perturbation $\Phi' = \psi' f_0$, the temperature perturbation and the vertical pressure velocity $\omega = -w^* p/H$ along the centre position y_0 on the f- and β-plane for their most unstable wave modes $\widetilde{k} = 10$ and $\widetilde{k} = 12$, respectively. Here, we are only interested in the general patterns of the QG wave perturbations in the (x, z^*) domain and leave out the secondary information about the actual amplitudes. The QG Figures 11 and 12 confirm the WRF and MCore simulation results from section 3.3 (Figures 7 and 8). Both the f- and β-plane perturbations of the QG geopotential and temperature fields agree well with the patterns of strongest development obtained from the simulations. In our QG analysis (Figures 11 and 12) the geopotential perturbations are inclined westwards with altitude, whereas the temperature shows a dominant eastward tilt with height, especially in the lower atmosphere. These patterns are also present in WRF and MCore. In addition, we observe in the QG results that the updraught regions ($\omega < 0$ Pa s^{-1}) are co-located with positive temperature anomalies, and both the updraught and warm regions are located between the low (to the west) and high (to the east) geopotential perturbations.

4.3. Power spectrum of the baroclinic instability

In order to better understand how well the linear QG theory represents the flow field, we now evaluate the wave-like nature of the baroclinic instability. In Figure 13 the zonal power spectrum of the MCore meridional velocity field is plotted at the centre position y_0 at the lowest model level (500 m) on both the f- and β-plane. A 15-day simulation time period is depicted which displays the $\log_{10}$ power amplitudes for the discrete wave numbers $\widetilde{k}$. The meridional velocity is directly connected to the geopotential perturbations via the geostrophic wind relationship. Since v is zero in the background, the meridional velocity only picks out the power of the growing disturbance, and is therefore an ideal candidate for the analysis. Figure 13 shows that the discrete wave number $\widetilde{k} = 10$ on the f-plane and $\widetilde{k} = 12$ on the β-plane experience the biggest power amplitudes and therefore the most rapid growth in MCore. This growth process is dominated by linear interactions until wave breaking occurs. Once wave breaking sets in, deposition occurs into smaller scales, as observed around day 13.5 on the f-plane and around day 11 on the β-plane. Due to the nature of the nonlinear interaction between wave modes, the system then sets up a series of resonances which inhibits the growth of certain discrete wave modes. This result is apparent in the Fourier spectra in Figure 13, especially on the β-plane, where gaps are clearly present in the power spectrum after day 9.

To assess whether the linear QG theory validates the growth rate of the most unstable mode in MCore, Figure 14 plots the amplitude versus time of the zonal Fourier power spectrum of the MCore meridional velocity at $\widetilde{k} = 10$ (f-plane, (a)) and $\widetilde{k} = 12$ (β-plane, (b)). The overlaid theoretical growth rate in Figure 14 is assessed using kc_i from Figure 9(b). As shown in (40), the growth of the unstable wave is proportional to the exponential form $\exp(kc_i t)$. Note that Figure 14 selects an arbitrary starting position (at $t = 0$ s) for the theoretical growth rate which lies in close proximity to the MCore growth curve. This draws attention to the steepness of the two slopes which
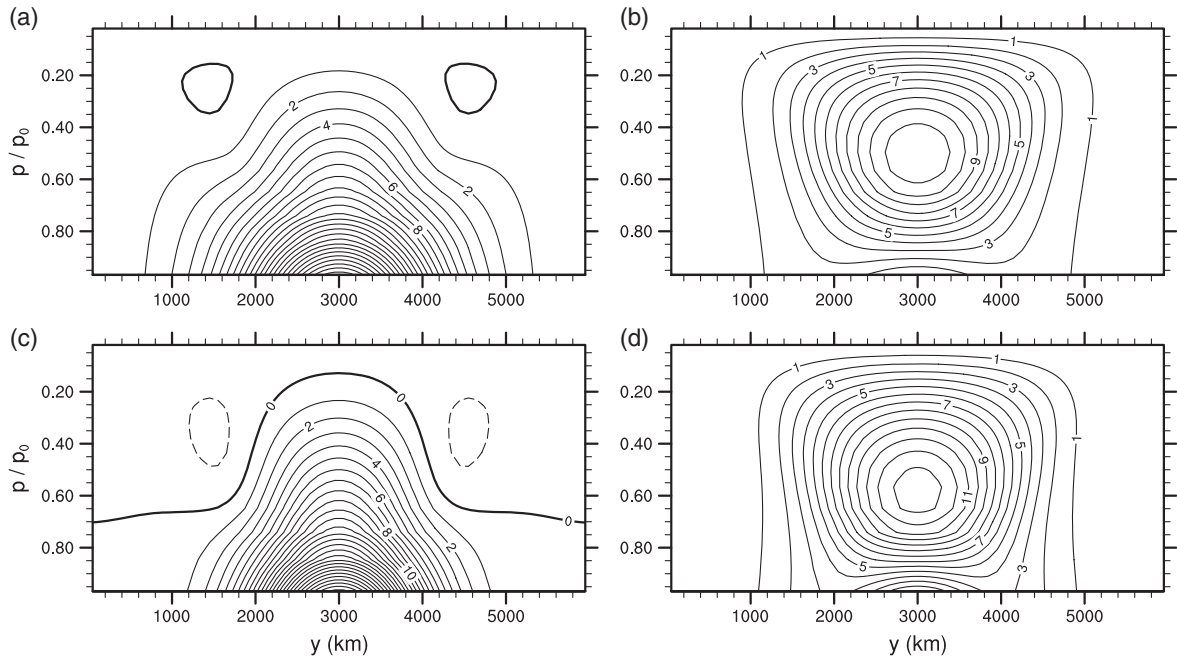
Figure 10. Meridional−vertical cross-sections of the (a,c) real and (b,d) imaginary components of the streamfunction amplitude function $\Psi(y,z^*)$ for the most unstable wave mode (a,b) $\widetilde{k} = 10$ on the f-plane and (c,d) $\widetilde{k} = 12$ on the β-plane. Negative contours are dashed and the units are $m^2\ s^{-1}$.

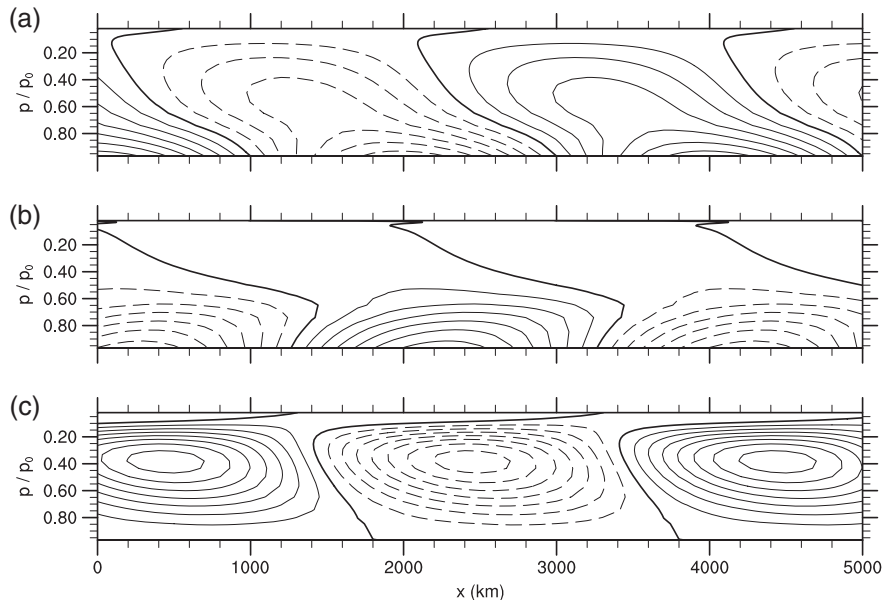**Figure 11.** Zonal−vertical cross-sections at the centre position y_0 of the (a) geopotential, (b) temperature and (c) vertical pressure velocity perturbations for the most unstable mode $\widetilde{k} = 10$ on the f-plane. Negative contours are dashed and the zero line is enhanced.

is the important piece of information here. Since the vertical axis is logarithmic, an exponential growth appears as a straight line. Figure 14 highlights the impressive agreement between the predicted growth rate from the linear QG theory and the growth rate obtained from the MCore simulation in the 'linear regime' prior to wave breaking. The reason for the different modelled and theoretical slopes during the early phases is that a variety of growing wave modes with similar power are present in MCore before the most unstable wave mode dominates. After the wave has broken, there is a clear loss of power associated with a transfer to finer scales, and consequently a deviation from the theoretically predicted growth rate. This also marks the time that is associated with enhanced gravity wave activity due to the nonlinear breaking of the baroclinic wave.

4.4. Theoretical considerations

In this section, we discuss the connection of our analysis to the theory of baroclinic instability. Notably, it is interesting that the

most unstable wave modes for f- and β-plane configurations (Figures 11 and 12) are in rough qualitative agreement with the most unstable mode of the Eady model (Eady, 1949), which is even more idealized than our QG analysis (see also textbooks such as Holton, 2004; Vallis, 2006). The maximum vertical velocity occurs at roughly $\eta = 0.4$ ($z^* = 7\,km$) in both cases, below the upper-atmospheric centre position of the zonal jet (Figures 7 and 8). The Eady model makes use of a rigid lid which assists the generation of the instability via so-called edge waves that propagate along the surface and rigid lid. However, the instability generated in our case is not sensitive to the altitude of the model top (above at least 20 km), and it is apparent that the unstable modes do not exhibit the vertical symmetry present in the Eady model. Further, the Eady model is known for a short-wave cut-off which suppresses instability at the highest wavenumbers, whereas these simulations appear to exhibit no such cut-off (Figure 9). This may suggest that the test case in this article is more closely connected with the Charney model (Charney, 1947) (which has no cut-off), and inspection of Figure 2 reveals that our
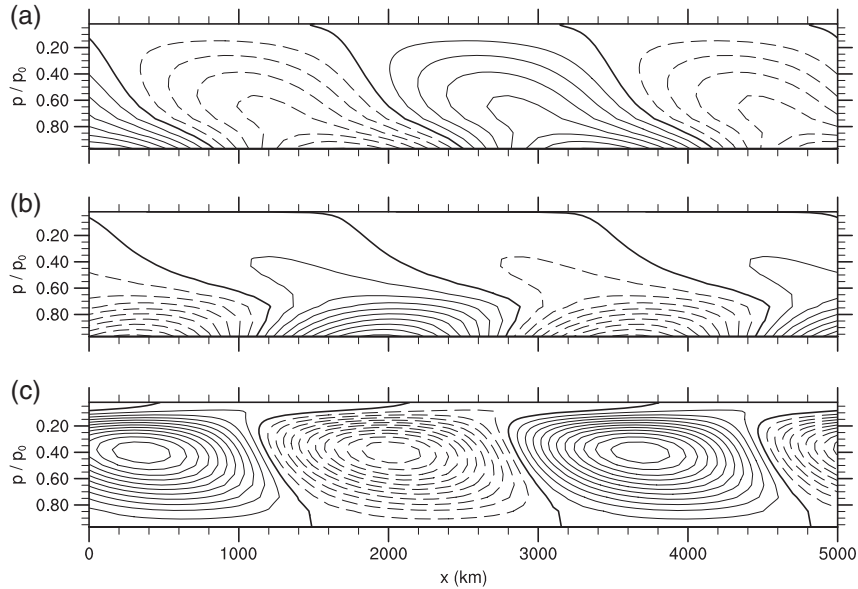
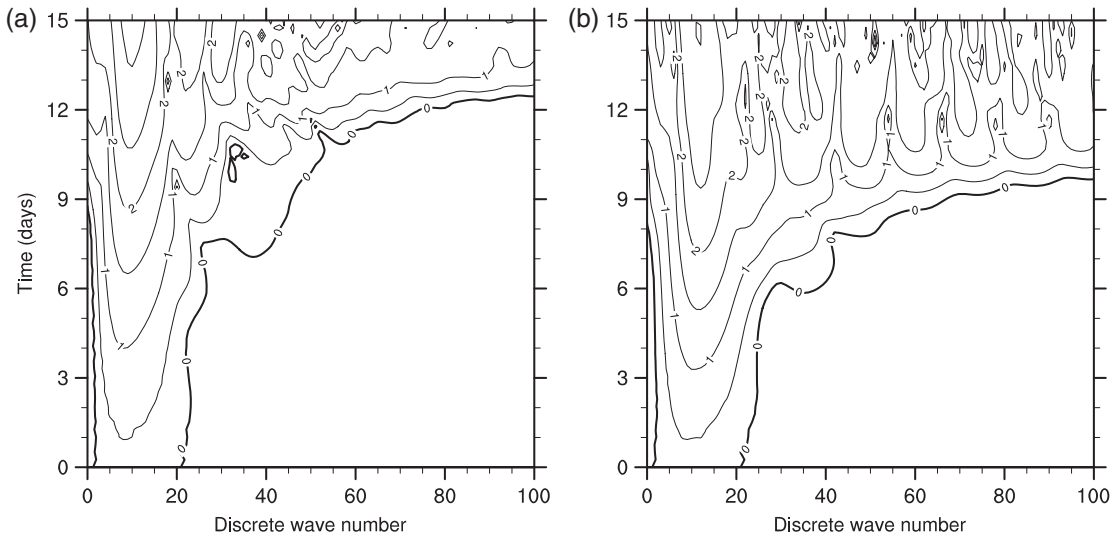**Figure 12.** As Figure 11, but for $\widetilde{k} = 12$ on the β-plane.

Figure 13. Dependence of the zonal Fourier power spectrum of the MCore meridional velocity at the centre position y_0 and lowest model level (500 m) on the discrete wave number $\widetilde{k}$. The contours show the $\log_{10}$ of the power spectra on the (a) f-plane and (b) β-plane over the 15-day simulation period.

initial conditions exhibit an internal PV gradient–whose strength varies between the f and β cases–which is absent in the Eady formulation.

In fact, the most rigorous theory describing the behaviour of baroclinic instability is derived by Heifetz *et al.* (2004a), using counter-propagating Rossby waves (CRWs)–that is, upper and lower wave modes whose counter-propagation relative to the mean flow leads to resonant growth. The theory builds on earlier work by Bretherton (1966), who extended Eady's two-layer model to include a QG PV gradient and showed this framework could be used to capture the basic nature of the instability. Note that the QG theory itself does not apply directly to our initialization, since the stability parameter σ that appears in QG theory has significant variation in the y direction when computed from Eqs (1)−(10).
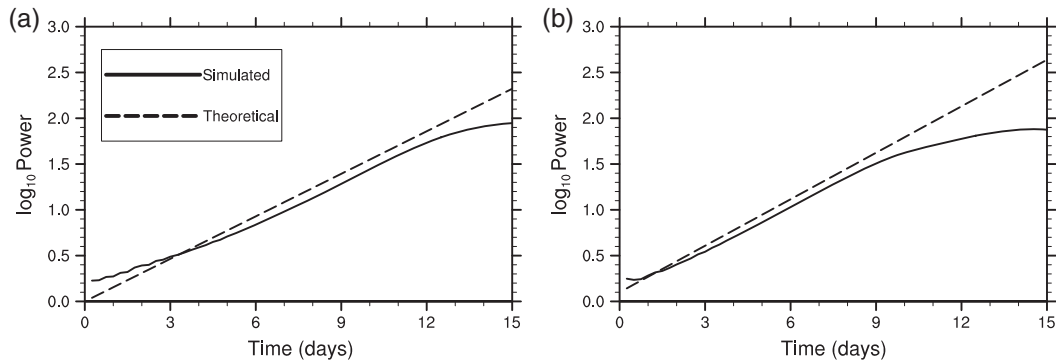

Figure 14. Power amplitude of the most unstable wave modes (a) $\widetilde{k} = 10$ on the f-plane and (b) $\widetilde{k} = 12$ on the β-plane over a 15-day simulation. The solid line shows the $\log_{10}$ of the zonal Fourier power spectrum of the MCore meridional velocity from Figure 13. The theoretically predicted maximum growth rate, as derived from the linear QG theory, is shown by the dashed line.

Nonetheless, over short time-scales, when the horizontal gradient of σ is perpendicular to the geostrophic wind, the QG theory will hold approximately. Using a spatially variable σ parameter, the meridional gradient of QG PV changes sign from negative in the lower model levels to positive in the upper model levels (not shown). The CRW theory notes that unstable baroclinic modes in the Eady model are supported only due to the boundaries, whereas in the Charney model these modes can exist due to the presence of an interior PV gradient (Heifetz *et al.*, 2004b). The applicability of the CRW theory to our results is apparent when comparing (our) Figure 10 with Figure 3 of Methven *et al.* (2005) and (our) Figures 7(d) and 8(d) with Figure 4e of Methven *et al.* (2005). It is apparent that Figure 10 actually shows the structure of the lower and upper CRWs associated with the prescribed background state, and exhibits westward-tilted behaviour consistent with the CRW theory.

5. Conclusions

In this article we have introduced idealized initial conditions for the simulation of baroclinic instability waves in 3D atmospheric channel models. The unique aspect of the initial conditions is that they are analytical for both an f- and β-plane configuration with only very minor differences in the initial states. The initial conditions and the evolving baroclinic waves are qualitatively very similar to those of a real atmosphere, which makes the initial state appealing for both numerical and physical science investigations.

First, the initial conditions can be considered a 'baroclinic wave test case' to assess the numerical characteristics of 3D Cartesian channel models. In particular, a steady-state configuration can be used as a first step for numerical convergence studies, before selecting the baroclinic wave configuration as a debugging or model intercomparison tool. Channel models are typically part of the model development hierarchy that consists of 2D $(x−y)$ shallow-water, 2D $(x−z)$ Cartesian channel, 3D Cartesian channel and 3D dynamical cores on the sphere. A variety of non-trivial (non-isothermal, non-state-at-rest) test cases with analytical initial conditions exist in the literature for all model categories except for 3D Cartesian channel models. The only exception is the work by Staniforth (2012) who proposed exact stationary solutions of the Euler equations on $\beta−\gamma$ planes. In addition, Wang and Polvani (2011) provided a complete description of their balanced initial datasets on the f-plane which require only very basic numerical integrations, but more complex iterations to obtain the normal-mode perturbation. The typical assessments of baroclinic instability flows in 3D channels are based on initial data which heavily rely on numerical techniques for the PV inversion. Since these techniques are generally not fully documented, the results cannot be reproduced by others. Our approach guarantees reproducibility and helps fill this crucial gap. In addition, we provide a 'recipe' on how to generate other analytical initial conditions, with e.g. additional meridional zonal wind shear or moisture (Appendix C), to broaden the range of science questions. In order to provide examples of the flow field, we compared the evolution of the baroclinic wave in the two non-hydrostatic channel models MCore (Ullrich and Jablonowski, 2012) and WRF (Skamarock *et al.*, 2008). The baroclinic waves closely resembled each other, which suggests that the numerical solutions are trustworthy and provide a point of comparison for other modellers.

Second, the initial conditions also lay the groundwork for interesting physical science questions, such as the impact of the varying f- and β-plane Coriolis parameter on the flow field, which is a central point of this article. Our f- and β-plane simulations use very similar initial data fields with identical vertical wind shear and almost identical static stability. These are factors that are known for their impact on the growth of unstable baroclinic waves. The numerical experiments showed that the evolution of the baroclinic wave on the β-plane is more unstable than the corresponding f-plane configuration, experiencing a faster linear growth rate of the most unstable wave mode, a shorter most unstable wavelength, a narrower meridional width, and an earlier breaking of the baroclinic wave. A theoretical analysis based on QG theory sheds light on these findings and furthermore validates the numerical simulations. The simulated baroclinic instability waves on both the f- and β-plane matched the predicted wavelength, shape and linear growth rate obtained from the QG theory very well. Our results also suggest that the dynamics within a continuously stratified baroclinic instability differ from the results of a two-layer model of baroclinic instability. In the two-layer theory, the addition of β tends to stabilize the flow, especially the very long waves, and reduces the corresponding instability. Our results with the most unstable wave modes between $\widetilde{k} = 10$ and 12 show that the β-plane is more unstable. However, our results also show that the growth rates of longer waves with $\widetilde{k} < 10$ are smaller in the β-plane simulation, which is in general agreement with the two-layer QG theory.

Appendix A

Vertical η coordinate

The hybrid terrain-following η-coordinate (Simmons and Burridge, 1981) comprises a pure pressure coordinate and a σ-component with $\sigma = p/p_s$. The pressure p at a vertical model level η is given by

$$p(x, y, \eta, t) = a(\eta) p_0 + b(\eta) p_s(x, y, t), \qquad (A1)$$

where the hybrid coefficients $a(\eta)$ and $b(\eta)$ are height-dependent and most often provided in tabular form (e.g. Reed and Jablonowski, 2012, for the 30-level configuration of NCAR's Community Atmosphere Model (CAM) version 5). We recommend choosing a set-up with $p_0 = 10^5$ Pa and constant initial surface pressure $p_s = p_0$. This leads to the simplified expression

$$p(x, y, \eta, t = 0) = \{a(\eta) + b(\eta)\} p_0 = \eta\, p_0 . \qquad (A2)$$

In the discrete representation, the vertical direction is subdivided into N_{lev} model levels which are bounded by $N_{lev} + 1$ interface levels (denoted by the half indices $k + \frac{1}{2}$). The pressure at the interfaces is then given by

$$p_{k+\frac{1}{2}} = a_{k+\frac{1}{2}} p_0 + b_{k+\frac{1}{2}} p_s = \eta_{k+\frac{1}{2}} p_0, \qquad (A3)$$

with $\eta_{k+\frac{1}{2}} = a_{k+\frac{1}{2}} + b_{k+\frac{1}{2}}$ and $k = 0, 1, 2, \cdots N_{lev}$. The corresponding η_k values at the level centres (the full model levels) are determined via the average $\eta_k = \frac{1}{2} (\eta_{k+\frac{1}{2}} + \eta_{k-\frac{1}{2}})$. It follows $p_k = \eta_k p_0$.

Note that some GCMs (e.g. documented by Majewski *et al.*, 2002; Untch and Hortal, 2004) employ the alternative notation $p_{k+\frac{1}{2}} = a_{k+\frac{1}{2}} + b_{k+\frac{1}{2}} p_s$ where the coefficients $a_{k+\frac{1}{2}}$ are already multiplied with the reference surface pressure p_0 and given in Pa. If such coefficients are provided, special care needs to be taken to recover the η positions. First, the model-specific value of p_0 needs to be determined as some models utilize the 'standard atmosphere' value of 1.01325×10^5 Pa like Untch and Hortal (2004). Second, the pressure-based $a_{k+\frac{1}{2}}$ coefficients need to be divided by p_0 to yield the η coefficients at layer interfaces

$$\eta_{k+\frac{1}{2}} = \frac{a_{k+\frac{1}{2}}}{p_0} + b_{k+\frac{1}{2}}. \qquad (A4)$$

The latter can be linearly averaged as shown earlier to give the corresponding η value at a full model level.

Appendix B

Iterative method for channel models with z-based vertical coordinates

The initial conditions for the baroclinic wave in the 3D Cartesian channel have been designed for pressure-based vertical coordinates with initially $\eta = \sigma = p/p_s$. For models with height-based vertical coordinates, we suggest using Newton's method which is a root-finding technique. It yields the corresponding η-level for any desired z position to machine precision. Newton's method therefore avoids vertical interpolations of the initial dataset and furthermore is easy to implement. The algorithm has already been described for e.g. baroclinic wave initial conditions on the sphere by Jablonowski and Williamson (2006a) (their Appendix) and is briefly summarized here for completeness. In particular, the iterative method is given by

$$\eta^{n+1} = \eta^n - \frac{F(x, y, \eta^n)}{\frac{\partial F}{\partial \eta}(x, y, \eta^n)}, \tag{B1}$$

where the superscript $n = 0, 1, 2, 3, \ldots$ denotes the iteration count.

For a selected z-level of the height-based vertical coordinate, the functions F and $\partial F/\partial \eta$ are determined by

$$F(x, y, \eta^n) = -g z + \Phi(x, y, \eta^n), \tag{B2}$$

$$\frac{\partial F}{\partial \eta}(x, y, \eta^n) = -\frac{R_d}{\eta^n} T(x, y, \eta^n), \tag{B3}$$

where Φ and T are provided by Eqs. (6) and (9), respectively.

The starting value $\eta^0 = 10^{-7}$ is recommended for all Newton iterations following (B1) which corresponds to a model top of about 100 km. The convergence is achieved if η^0 is greater than zero and physically lies above the uppermost model level. Typically, Newton's method converges within a maximum of 25 iterations, and most often the convergence is already achieved in under ten iterations. Then the absolute error $|\eta - \eta^n|$ is decreased to machine precision. The resulting η-level for the location (x, y, z) can then be used for the computation of the analytical initial conditions at the location (x, y, η).

If the model requires the initialization of the pressure p, density ρ or potential temperature Θ, they can be computed as follows. First, determine $\eta(x, y, z)$ via the iterative technique. Second, determine p, ρ and Θ via

$$p(x, y, \eta) = \eta(x, y, z) p_0, \tag{B4}$$

$$\rho(x, y, \eta) = \frac{p(x, y, \eta)}{R_d T(x, y, \eta)}, \tag{B5}$$

$$\Theta(x, y, \eta) = T(x, y, \eta) \left\{ \frac{p_0}{p(x, y, \eta)} \right\}^{\frac{R_d}{c_p}}, \tag{B6}$$

with the specific heat at constant pressure $c_p = 1004.5 \, \text{J kg}^{-1}\text{K}^{-1}$.

Figure S1 depicts the initial zonal wind and relative vorticity with respect to the height coordinate. In addition, Figures S2 and S3 show the corresponding initial temperature, pressure, potential temperature, absolute vorticity, Brunt–Väisälä frequency and Ertel's potential vorticity for both the f- and β-plane. We provide these figures to accommodate non-hydrostatic models with z coordinates and allow a straightforward comparison of the initial dataset.

Appendix C

Inclusion of moisture

The analytical initial conditions for a moist variant of the baroclinic wave are almost identical to the dry configuration.

The differences are that the original T equation (9) is now the definition of the virtual temperature T_v, the originally dry surface pressure $p_s = p_0$ and geopotential are interpreted as the surface pressure and geopotential of the moist air, the definition of the density needs to utilize the virtual temperature, and an analytical expression for the specific humidity q is added. The wind initialization of the moist baroclinic wave is identical to the dry case.

A suggested zonally symmetric specific humidity field is

$$\langle q(\eta) \rangle = \frac{q_0}{2} \begin{cases} 1 + \cos\left[\frac{\pi(1-\eta)}{1-\eta_w}\right] & \text{if } \eta \geq \eta_w, \\ 0 & \text{otherwise,} \end{cases} \tag{C1}$$

$$q(x, y, \eta) = \langle q(\eta) \rangle \exp\left\{ -\left(\frac{y}{\Delta y_w}\right)^4 \right\}, \tag{C2}$$

with the meridional width parameter $\Delta y_w = 3200$ km, the η-based width parameter $\eta_w = 0.3$ and the maximum specific humidity amplitude $q_0 = 0.018 \, \text{kg kg}^{-1}$.

The density of the moist air is defined by the ideal gas law

$$\rho(x, y, \eta) = \frac{p(x, y, \eta)}{R_d T_v(x, y, \eta)} \tag{C3}$$

and utilizes the pressure p of the moist air. The formulation of the virtual temperature and specific humidity leads to the analytically balanced representation of the temperature

$$T(x, y, \eta) = \frac{T_v(x, y, \eta)}{1 + 0.608 \, q(x, y, \eta)}. \tag{C4}$$

This temperature is lower than the original dry temperature (Eq. (9)). However, note that in the moist case the virtual temperature and moist pressure determine the strength of the pressure gradient term in the momentum equations. Since these are identical to the temperature and pressure in the dry case, the forcing by the pressure gradient term is the same in both the dry and moist variant of the baroclinic wave. Once moisture is specified, the model simulation can be run with a simple large-scale condensation parametrization as in Reed and Jablonowski (2012), or using more complex physical parametrizations, to provide the precipitation and latent heating feedbacks.

Appendix D

Numerical discretization of Sturm–Liouville problem

We define a discrete mesh over the domain $[0, L_y] \times [0, z_{\text{top}}^*]$ via

$$y_j = \left(j - \frac{1}{2}\right) \Delta y, \quad \text{and} \quad z_k^* = \left(k + \frac{1}{2}\right) \Delta z^*, \tag{D1}$$

where $j \in \{1, \ldots, N_y\}$ and $k \in \{1, \ldots, N_z\}$ are y and z^* indices within the mesh, $\Delta y = L_y/N_y$ and $\Delta z^* = z_{\text{top}}^*/N_z$, and N_y and N_z denote the number of elements in each coordinate direction (chosen to be 60 and 30 in practice). Consequently, we define Ψ at $(y, z) = (y_j, z_k)$ as $\Psi_{j,k}$. Within the interior of the domain, (36) is discretized using central derivatives,

$$\left(\frac{\partial^2 \Psi}{\partial y^2}\right)_{j,k} \approx \frac{\Psi_{j+1,k} - 2\Psi_{j,k} + \Psi_{j-1,k}}{\Delta y}. \tag{D2}$$

The vertical derivative term is expanded as

$$\frac{1}{\rho_0} \frac{\partial}{\partial z^*}\left(\frac{f_0^2 \rho_0}{N^2} \frac{\partial \Psi}{\partial z^*}\right) = \frac{f_0^2}{N^2 \rho_0} \frac{\partial \rho_0}{\partial z^*} \frac{\partial \Psi}{\partial z^*} + \frac{f_0^2}{N^2} \frac{\partial^2 \Psi}{\partial (z^*)^2}, \tag{D3}$$

and each derivative term discretized as

$$\left(\frac{\partial^2 \Psi}{\partial (z^*)^2}\right)_{j,k} \approx \frac{\Psi_{j,k+1} - 2\Psi_{j,k} + \Psi_{j,k-1}}{(\Delta z^*)^2}, \qquad (D4)$$

$$\left(\frac{\partial \Psi}{\partial z^*}\right)_{j,k} \approx \frac{\Psi_{j,k+1} - \Psi_{j,k-1}}{2\Delta z^*}. \qquad (D5)$$

At lateral boundaries we enforce the no-flux condition $\Psi = 0$, and so the second derivative in y becomes

$$\left(\frac{\partial^2 \Psi}{\partial y^2}\right)_{1,k} \approx \frac{-12\Psi_{1,k} + 4\Psi_{2,k}}{3\Delta y^2}, \qquad (D6)$$

$$\left(\frac{\partial^2 \Psi}{\partial y^2}\right)_{N_y,k} \approx \frac{-12\Psi_{N_y,k} + 4\Psi_{N_y-1,k}}{3\Delta y^2}. \qquad (D7)$$

At vertical boundaries we must enforce (37). By writing the vertical derivative terms at the lower boundary as

$$\left(\frac{\partial \Psi}{\partial z^*}\right)_{j,1} \approx \frac{1}{2}\left(\frac{\partial \Psi}{\partial z^*}\right)_{j,1/2} + \frac{1}{2}\left(\frac{\partial \Psi}{\partial z^*}\right)_{j,3/2}, \qquad (D8)$$

$$\left(\frac{\partial^2 \Psi}{\partial (z^*)^2}\right)_{j,1} \approx \frac{1}{\Delta z^*}\left\{\left(\frac{\partial \Psi}{\partial z^*}\right)_{j,3/2} - \left(\frac{\partial \Psi}{\partial z^*}\right)_{j,1/2}\right\}, \qquad (D9)$$

where half-indices denote element edges, we note that we can express the cell-centred vertical derivative in terms of a derivative across the upper edge and one at the boundary. Again using a centred approximation,

$$\left(\frac{\partial \Psi}{\partial z^*}\right)_{j,3/2} \approx \frac{\Psi_{j,2} - \Psi_{j,1}}{\Delta z^*}, \qquad (D10)$$

and at the lower boundary

$$\left(\frac{\partial \Psi}{\partial z^*}\right)_{j,1/2} \approx \frac{1}{(\overline{u} - c)}\left(\frac{\partial \overline{u}}{\partial z^*}\right)_{j,1} \Psi_{j,1}. \qquad (D11)$$

A similar approximation is applied at the upper boundary. After applying all approximations, we rearrange (36) to obtain a matrix system of the form

$$\mathbf{A}\Psi_{\mathrm{d}} = c\mathbf{B}\Psi_{\mathrm{d}}, \qquad (D12)$$

where Ψ_{d} is the vectorized form of $\Psi_{j,k}$. Since $\mathbf{B}$ is invertible, this system can be written as an eigenvalue problem of the form

$$\mathbf{F}\Psi_{\mathrm{d}} = c\Psi_{\mathrm{d}}, \qquad (D13)$$

where $\mathbf{F} = \mathbf{B}^{-1}\mathbf{A}$. This system can then be solved using standard numerical linear algebra techniques as provided e.g. in Matlab.

Supporting information

Figure S1. The initial zonal wind and relative vorticity with respect to the height coordinate.
Figure S2. The corresponding initial temperature, pressure, potential temperature, absolute vorticity, Brunt–Väisälä frequency and Ertel's potential vorticity for the f-plane.
Figure S3. As Figure S2, but for the β-plane.

References

Bretherton F. 1966. Baroclinic instability and the short-wavelength cut-off in terms of potential vorticity. *Q. J. R. Meteorol. Soc.* **92**: 335–345.

Charney JG. 1947. The dynamics of long waves in a baroclinic westerly current. *J. Meteorol.* **4**: 136–162.
Davies DH, Schär C, Wernli H. 1991. The palette of fronts and cyclones within a baroclinic wave development. *J. Atmos. Sci.* **48**: 1666–1689.
Davis CA. 2010. Simulations of subtropical cyclones in a baroclinic channel model. *J. Atmos. Sci.* **67**: 2871–2892.
Eady E. 1949. Long waves and cyclone waves. *Tellus* **1**: 33–52.
Galewsky J, Polvani LM, Scott RK. 2004. An initial-value problem to test numerical models of the shallow-water equations. *Tellus* **56A**: 429–440.
Heifetz E, Bishop C, Hoskins BJ, Methven J. 2004a. The counter-propagating Rossby-wave perspective on baroclinic instability. I: Mathematical basis. *Q. J. R. Meteorol. Soc.* **130**: 211–231.
Heifetz E, Methven J, Hoskins BJ, Bishop C. 2004b. The counter-propagating Rossby-wave perspective on baroclinic instability. II: Application to the Charney model. *Q. J. R. Meteorol. Soc.* **130**: 233–258.
Holton JR. 2004. *An Introduction to Dynamic Meteorology* (4th edn). Academic Press, Inc.: Waltham, MA.
Jablonowski C, Williamson DL. 2006a. A baroclinic instabilitiy test case for atmospheric model dynamical cores. *Q. J. R. Meteorol. Soc.* **132**: 2943–2975.
Jablonowski C, Williamson DL. 2006b. 'A baroclinic wave test case for dynamical cores of general circulation models: Model intercomparisons', Technical Note NCAR/TN-469+STR. National Center for Atmospheric Research: Boulder, CO, doi: 10.5065/D6765C86.
Kasahara A. 1974. Various vertical coordinate systems used for numerical weather prediction. *Mon. Weather Rev.* **102**: 509–522.
Laprise R. 1992. The Euler equations of motion with hydrostatic pressure as an independent variable. *Mon. Weather Rev.* **120**: 197–207.
Majewski D, Liermann D, Prohl P, Ritter B, Buchhold M, Hanisch T, Paul G, Wergen W, Baumgardner J. 2002. The operational global icosahedral–hexagonal gridpoint model GME: Description and high-resolution tests. *Mon. Weather Rev.* **130**: 319–338.
Methven J, Heifetz E, Hoskins B, Bishop C. 2005. The counter-propagating Rossby-wave perspective on baroclinic instability. Part III: Primitive-equation disturbances on the sphere. *Q. J. R. Meteorol. Soc.* **131**: 1393–1424.
Mirzaei M, Zülicke C, Mohebalhojeh AR, Ahmadi-Givi F, Plougonven R. 2014. Structure, energy, and parameterization of inertia-gravity waves in dry and moist simulations of a baroclinic wave life cycle. *J. Atmos. Sci.* **71**: 2390–2414.
Phillips NA. 1957. A coordinate system having some special advantages for numerical forecasting. *J. Meteorol.* **14**: 184–185.
Plougonven R, Snyder C. 2007. Inertia-gravity waves spontaneously generated by jets and fronts. Part I: Different baroclinic life cycles. *J. Atmos. Sci.* **64**: 2502–2520.
Reed KA, Jablonowski C. 2012. Idealized tropical cyclone simulations of intermediate complexity: A test case for AGCMs. *J. Adv. Model. Earth Syst.* **4**: M04001, doi: 10.1029/2011MS000099.
Rotunno R. 1994. An analysis of frontogenesis in numerical simulations of baroclinic waves. *J. Atmos. Sci.* **51**: 3373–3398.
Schär C, Wernli H. 1993. Structure and evolution of an isolated semi-geostrophic cyclone. *Q. J. R. Meteorol. Soc.* **119**: 57–90.
Simmons AJ, Burridge DM. 1981. An energy and angular-momentum conserving vertical finite-difference scheme and hybrid vertical coordinates. *Mon. Weather Rev.* **109**: 758–766.
Simmons AJ, Hoskins BJ. 1978. The life cycles of some nonlinear baroclinic waves. *J. Atmos. Sci.* **35**: 414–432.
Skamarock WC, Klemp JB, Dudhia J, Gill DO, Barker DM, Duda MG, Huang XY, Wang W, Powers JG. 2008. 'A description of the advanced research WRF version 3', Technical Note NCAR/TN-475+STR. National Center for Atmospheric Research: Boulder, CO.
Staniforth A. 2012. Exact stationary axisymmetric solutions of the Euler equations on β–γ planes. *Atmos. Sci. Lett.* **13**: 79–87.
St-Cyr A, Jablonowski C, Dennis J, Thomas S, Tufo H. 2008. A comparison of two shallow-water models with non-conforming adaptive grids. *Mon. Weather Rev.* **136**: 1898–1922.
Tan ZM, Zhang F, Rotunno R, Snyder C. 2004. Mesoscale predictability of moist baroclinic waves: Experiments with parameterized convection. *J. Atmos. Sci.* **61**: 1794–1804.
Terpstra A, Spengler T. 2015. An initialization method for idealized channel simulations. *Mon. Weather Rev.* **143**: 2043–2051, doi: 10.1175/MWR-D-14-00248.1.
Thorncroft CD, Hoskins BJ, McIntyre ME. 1993. Two paradigms of baroclinic-wave life-cycle behaviour. *Q. J. R. Meteorol. Soc.* **119**: 17–55.
Ullrich PA, Jablonowski C. 2012. Operator-split Runge–Kutta–Rosenbrock (RKR) methods for non-hydrostatic atmospheric models. *Mon. Weather Rev.* **140**: 1257–1284.
Ullrich PA, Melvin T, Jablonowski C, Staniforth A. 2014. A proposed baroclinic wave test case for deep- and shallow-atmosphere dynamical cores. *Q. J. R. Meteorol. Soc.* **140**: 1590–1602.
Untch A, Hortal M. 2004. A finite-element scheme for the vertical discretization of the semi-Lagrangian version of the ECMWF forecast model. *Q. J. R. Meteorol. Soc.* **130**: 1505–1530.

Vallis GK. 2006. *Atmospheric and Oceanic Fluid Dynamics*. Cambridge University Press: Cambridge, UK.

Waite ML, Bartello P. 2006. The transition from geostrophic to stratified turbulence. *J. Fluid Mech.* **568**: 89−108.

Waite ML, Snyder C. 2009. The mesoscale kinetic energy spectrum of a baroclinic life cycle. *J. Atmos. Sci.* **66**: 883−901.

Waite ML, Snyder C. 2013. Mesoscale energy spectra of moist baroclinic waves. *J. Atmos. Sci.* **70**: 1242−1256.

Wang S, Polvani LM. 2011. Double tropopause formation in idealized baroclinic life cycles: The key role of an initial tropopause inversion layer. *J. Geophys. Res. (Atmos.)* **116**: D05108, doi: 10.1029/2010JD015118.

Weller H, Thuburn J, Cotter CJ. 2012. Computational modes and grid imprinting on five quasi-uniform spherical C-grids. *Mon. Weather Rev.* **140**: 2734−2755.

Zhang F. 2004. Generation of mesoscale gravity waves in upper-tropospheric jet-front systems. *J. Atmos. Sci.* **61**: 440−457.